



# JWST Reveals CO Ice, Concentrated CO<sub>2</sub> Deposits, and Evidence for Carbonates Potentially Sourced from Ariel's Interior

Richard J. Cartwright<sup>1</sup> , Bryan J. Holler<sup>2</sup> , William M. Grundy<sup>3,4</sup> , Stephen C. Tegler<sup>4</sup> , Marc Neveu<sup>5,6</sup> , Ujjwal Raut<sup>7</sup> , Christopher R. Glein<sup>7</sup> , Tom A. Nordheim<sup>1</sup> , Joshua P. Emery<sup>4</sup> , Julie C. Castillo-Rogez<sup>8</sup> , Eric Quirico<sup>9</sup> , Silvia Protopapa<sup>10</sup> , Chloe B. Beddingfield<sup>1</sup> , Matthew M. Hedman<sup>11</sup> , Katherine de Kleer<sup>12</sup> , Riley A. DeColibus<sup>8</sup> , Anastasia N. Morgan<sup>4</sup> , Ryan Wochner<sup>4</sup> , Kevin P. Hand<sup>8</sup> , Geronimo L. Villanueva<sup>6</sup> , Sara Faggi<sup>6,13</sup> , Noemi Pinilla-Alonso<sup>14</sup> , David E. Trilling<sup>4</sup> , and Michael M. Mueller<sup>15</sup>

<sup>1</sup> Johns Hopkins University Applied Physics Laboratory, 11101 Johns Hopkins Rd, Laurel, MD 20723, USA; richard.cartwright@jhuapl.edu

<sup>2</sup> Space Telescope Science Institute, 3700 San Martin Drive, Baltimore, MD 21218, USA

<sup>3</sup> Lowell Observatory, 1400 W. Mars Hill Road, Flagstaff, AZ 86001, USA

<sup>4</sup> Department of Astronomy and Planetary Science, Northern Arizona University, 527 S. Beaver Street, Flagstaff, AZ 86011, USA

<sup>5</sup> University of Maryland, 4296 Stadium Dr., College Park, MD 20742, USA

<sup>6</sup> Solar System Exploration Division, NASA Goddard Space Flight Center, 8800 Greenbelt Road, Greenbelt, MD 20771, USA

<sup>7</sup> Southwest Research Institute, 6220 Culebra Road, San Antonio, TX 78238-5166, USA

<sup>8</sup> Jet Propulsion Laboratory, California Institute of Technology, 4800 Oak Grove Drive, Pasadena, CA 91109, USA

<sup>9</sup> Institut de Planétologie et d'Astrophysique (IPAG), UMR 5274, CNRS, Université Grenoble Alpes, Grenoble, France

<sup>10</sup> Southwest Research Institute, 1301 Walnut Street, Boulder, CO 80302, USA

<sup>11</sup> Department of Physics, University of Idaho, 375 Perimeter Drive, MS 0903, Moscow, ID 83843, USA

<sup>12</sup> Division of Geological and Planetary Sciences, California Institute of Technology, 1200 E. California Boulevard, Pasadena, CA 91125, USA

<sup>13</sup> American University, 4400 Massachusetts Avenue NW, Washington, DC 20016, USA

<sup>14</sup> Florida Space Institute, University of Central Florida, 12354 Research Pkwy., Orlando, FL 32826, USA

<sup>15</sup> Kapteyn Astronomical Institute Rijksuniversiteit Groningen, P.O. Box 800, 9700 AV Groningen, The Netherlands

Received 2024 May 7; revised 2024 June 8; accepted 2024 June 9; published 2024 July 24

## Abstract

The Uranian moon Ariel exhibits a diversity of geologically young landforms, with a surface composition rich in CO<sub>2</sub> ice. The origin of CO<sub>2</sub> and other species, however, remains uncertain. We report observations of Ariel's leading and trailing hemispheres, collected with NIRSpec (2.87–5.10 μm) on the James Webb Space Telescope. These data shed new light on Ariel's spectral properties, revealing a double-lobed CO<sub>2</sub> ice scattering peak centered near 4.20 and 4.25 μm, with the 4.25 μm lobe possibly representing the largest CO<sub>2</sub> Fresnel peak yet observed in the solar system. A prominent 4.38 μm <sup>13</sup>CO<sub>2</sub> ice feature is also present, as is a 4.90 μm band that results from <sup>12</sup>CO<sub>2</sub> ice. The spectra reveal a 4.67 μm <sup>12</sup>CO ice band and a broad 4.02 μm band that might result from carbonate minerals. The data confirm that features associated with CO<sub>2</sub> and CO are notably stronger on Ariel's trailing hemisphere compared to its leading hemisphere. We compared the detected CO<sub>2</sub> features to synthetic spectra of CO<sub>2</sub> ice and mixtures of CO<sub>2</sub> with CO, H<sub>2</sub>O, and amorphous carbon, finding that CO<sub>2</sub> could be concentrated in deposits thicker than ~10 mm on Ariel's trailing hemisphere. Comparison to laboratory data indicates that CO is likely mixed with CO<sub>2</sub>. The evidence for thick CO<sub>2</sub> ice deposits and the possible presence of carbonates on both hemispheres suggests that some carbon oxides could be sourced from Ariel's interior, with their surface distributions modified by charged particle bombardment, sublimation, and seasonal migration of CO and CO<sub>2</sub> from high to low latitudes.

*Unified Astronomy Thesaurus concepts:* Carbon dioxide (196); Ice spectroscopy (2250); Surface ices (2117); Surface processes (2116); Surface composition (2115); James Webb Space Telescope (2291); Uranian satellites (1750)

## 1. Introduction

Ariel is a candidate ocean world (e.g., Hendrix et al. 2019; Castillo-Rogez et al. 2023), with a young surface (<1 Ga in some regions; Kirchoff et al. 2022), exhibiting large chasmata and putative cryovolcanic features (e.g., Smith et al. 1986; Beddingfield & Cartwright 2021; Beddingfield et al. 2022). Ground-based telescope studies determined that the surfaces of Ariel and the other large Uranian moons are composed of H<sub>2</sub>O ice mixed with a neutral absorber analogous to amorphous carbon (e.g., Cruikshank et al. 1977; Brown &

Cruikshank 1983; Clark & Lucey 1984), overprinted by deposits of “pure” CO<sub>2</sub> ice (Grundy et al. 2003, 2006; Cartwright et al. 2015, 2022), and possible ammonia (NH<sub>3</sub>) bearing compounds (e.g., Bauer et al. 2002; Cartwright et al. 2018, 2020a, 2023; DeColibus et al. 2022, 2023).

Because of the high obliquity of the Uranus system (~98°), the subsolar point migrates between 82° south and 82° north over the course of Uranus's orbit, exposing the summer poles of its moons to constant sunlight (estimated peak temperatures 80–90 K; Hanel et al. 1986; Sori et al. 2017) while blocking sunlight from reaching their winter poles (20–30 K; Sori et al. 2017), for about 21 yr each season. At the estimated peak temperatures during spring and summer, CO<sub>2</sub> can sublimate and likely migrates to the winter hemisphere. Integrating this process over many seasons, the predicted outcome is to strip the poles of CO<sub>2</sub> and other volatiles and concentrate them at



Original content from this work may be used under the terms of the [Creative Commons Attribution 4.0 licence](#). Any further distribution of this work must maintain attribution to the author(s) and the title of the work, journal citation and DOI.

low latitudes, where diurnal variations in heating reduce sublimation rates (Grundy et al. 2006; Sori et al. 2017; Steckloff et al. 2022; Menten et al. 2023). Over time, CO<sub>2</sub> should be gradually lost to space owing to Jeans escape and magnetospheric interactions, depleting surface deposits, potentially enriching heavy isotopes, and raising the possibility that CO<sub>2</sub> is actively replenished.

By analogy to surface irradiation of the Galilean satellites and Saturn's midsized moons, radiolytic generation of CO<sub>2</sub> and other species might occur on the Uranian satellites (Grundy et al. 2003, 2006; Cartwright et al. 2015). Such a process might explain the stronger CO<sub>2</sub> “triplet” band (1.9–2.1 μm) on the trailing hemispheres of the largest Uranian moons and its weakening with increasing orbital distance (i.e., strongest on Ariel, weakest on Oberon). Nevertheless, predictions of moon-magnetosphere interactions at Uranus are not well constrained, and perhaps CO<sub>2</sub> is native and sourced from these moons’ interiors, with larger deposits on their trailing sides due to enhancement by radiolysis, similar to the multiple origin scenarios proposed for CO<sub>2</sub> on Jupiter’s moon Callisto (e.g., Hibbitts et al. 2000, 2002; J. M. Moore et al. 2004; Cartwright et al. 2024).

Irradiation of CO<sub>2</sub> should also generate other species, including CO (e.g., Bennett et al. 2010b; Raut et al. 2012; Raut & Baragiola 2013; Mifsud et al. 2022), carbon suboxide (C<sub>3</sub>O<sub>2</sub>; e.g., Strazzulla et al. 2007), and perhaps the cyanate ion (OCN<sup>-</sup>) and other CN-bearing compounds, assuming that CO<sub>2</sub> can interact with NH<sub>3</sub> and H<sub>2</sub>O (e.g., Hudson et al. 2001). Supporting this scenario, some ground-based spectra of Ariel exhibit a 2.35 μm band, tentatively attributed to CO ice (Cartwright et al. 2022). While hitherto undetected, hydrogen peroxide (H<sub>2</sub>O<sub>2</sub>) may be present on Ariel, forming from irradiation of H<sub>2</sub>O, similar to Europa (e.g., Carlson et al. 1999) and Charon (Protopapa et al. 2023, 2024). Laboratory experiments demonstrate that H<sub>2</sub>O<sub>2</sub> formation is more efficient in H<sub>2</sub>O ice mixed with a small fraction of CO<sub>2</sub> (<9%; Mamo et al. 2023), potentially making the Uranian moons’ surfaces ideal for H<sub>2</sub>O<sub>2</sub> production.

Unlike the CO<sub>2</sub> triplet band, subtle features between 2.12 and 2.27 μm attributed to NH<sub>3</sub>-bearing species and ammonium salts (hereafter referred to as the “2.2 μm band”) do not display discernible hemispherical or orbital trends. Instead, their variable band strengths suggest association with local-scale geologic features and terrains that cannot be resolved in the available disk-integrated data sets (Cartwright et al. 2020a, 2023; DeColibus et al. 2023). If NH<sub>3</sub>-bearing species are present, they are likely replenished over short timescales, due to the predicted rapid decomposition of NH<sub>3</sub> by magnetospheric charged particles (~10<sup>6</sup> yr at Miranda; Moore et al. 2007). The short life span of NH<sub>3</sub> and the possible association between geologic features and the 2.2 μm band on Ariel could result from recent exposure of NH<sub>3</sub>-rich deposits (Cartwright et al. 2020a). However, the ancient surface of the neighboring moon Umbriel (~4.5 Ga; Kirchoff et al. 2022) displays 2.2 μm bands as well, raising the possibility that more refractory components are contributing, such as carbonates, phyllosilicates, and organic residues (Cartwright et al. 2023).

To investigate the nature and origin of CO<sub>2</sub> ice and determine whether NH<sub>3</sub>-bearing species and other constituents are present, we measured spectra of Ariel with the NIRSpec spectrograph on the James Webb Space Telescope (JWST). These observations span an important wavelength range for

detecting CO<sub>2</sub> and CO (4.2–5.0 μm), NH-bearing species (2.9–3.2 μm), hydrocarbons (3.2–3.7 μm), nitriles (4.3–4.8 μm), carbonates (3.9–4.1 μm), and H<sub>2</sub>O<sub>2</sub> (~3.51 μm).

## 2. Data and Methods

**NIRSpec Observations:** As part of General Observer (GO) Program 1786, NIRSpec on JWST (Jakobsen et al. 2022; Böker et al. 2023) observed Ariel with the G395M/F290LP grating (2.87–5.10 μm, resolving power  $R \sim 1000$ ) on 2023 September 6 and 7, when the mid-observation, subobserver longitude was near 293° west (trailing hemisphere) and 63° west (leading hemisphere), respectively (subobserver latitude ~64.5° north for both observations). Each observation consisted of four dithers with NIRSpec’s integral field unit (IFU), for a total of ~3735 s (leading hemisphere) and ~3793 s (trailing hemisphere) of on-target time, using the NRSIRS2-RAPID readout mode. The data were downloaded from the Mikulski Archive for Space Telescopes ([10.17909/cwsn-7z50](https://doi.org/10.17909/cwsn-7z50)) (data reduction procedures described in Appendix A.1).

**Band Measurements:** We measured the band areas and depths of detected absorption features and scattering peaks using a band measurement program that defines and divides off a local linear continuum for each feature (e.g., Cartwright et al. 2024). Depth and height measurements were made by averaging the reflectance values within ±0.002 to 0.003 μm of a user-defined band ( $B_c$ ) or peak ( $P_c$ ) center, and uncertainties were computed using standard error propagation procedures (e.g., Taylor 1997). The spectral contrast for each absorption band ( $1 - B_d$ ) and scattering peak ( $P_d - 1$ ) was then measured. The trapezoidal rule was used to measure the area of each feature, using Monte Carlo simulations sampling the 1σ errors for data points within each feature to estimate errors (Table 1).

**Comparison to Synthetic and Laboratory Spectra:** We compared Ariel’s spectral properties to one-layer Hapke–Mie spectral models (Appendix A.2) generated using three sets of laboratory-derived indices of refraction (“optical constants”) for crystalline CO<sub>2</sub> ice measured at 150 K (Hansen 1997), 70 K (Gerakines & Hudson 2020), and 21 K (Quirico & Schmitt 1997a, 1997b) and for crystalline CO ice measured at 20 K (Robert Brown, private communication; Gerakines et al. 2023). Particulate and areal mixtures of CO<sub>2</sub>, CO, H<sub>2</sub>O, and amorphous C are shown in Figure A1.

We present absorbance spectra of CO + CO<sub>2</sub> ice mixtures measured in the Astrophysical Materials Laboratory at Northern Arizona University (Tegler et al. 2024). These co-condensed ices were made by mixing CO and CO<sub>2</sub> gases at room temperature before condensing as thin films on a gold mirror held at 20 K (see Tegler et al. 2024; Grundy et al. 2024a, for more details on laboratory procedures). We also compared the Ariel data to spectra of radiolyzed CO<sub>2</sub> ices processed by 100 keV protons (Raut & Baragiola 2013).

## 3. Results and Analyses

### 3.1. Detected Spectral Features

**CO<sub>2</sub> Ice:** The NIRSpec data exhibit a large scattering peak centered near 4.20 μm on Ariel’s leading and trailing hemispheres, flanked by an absorption band centered near 4.27 μm, and the trailing hemisphere shows an additional peak near 4.25 μm (Figure 1). All of these features are associated with the asymmetric stretch fundamental ( $\nu_3$ ) mode of <sup>12</sup>CO<sub>2</sub> (Figure 2).

**Table 1**  
Band Measurements for Ariel

| Feature Name                      | Feature Center ( $\mu\text{m}$ ) | Feature Wavelength Range ( $\mu\text{m}$ ) | Hemisphere | Spectral Contrast (%) | Band Area ( $10^{-4} \mu\text{m}$ ) | >3 $\sigma$ Spectral Contrast and Band Area? | Constituents   |
|-----------------------------------|----------------------------------|--|------------|-----------------------|-------------------------------------|--|--|
| <sup>a</sup> 3.10 $\mu\text{m}$   | 3.100                            | 3.014–3.168                                | Leading    | 99.29 $\pm$ 1.29      | 564.08 $\pm$ 2.07                   | Yes  | <b>H<sub>2</sub>O Ice</b>  |
|                                   |                                  |  | Trailing   | 68.37 $\pm$ 0.90      | 388.65 $\pm$ 1.68                   | Yes  |  |
| 3.33 $\mu\text{m}$                | 3.331                            | 3.308–3.362                                | Leading    | -0.65 $\pm$ 0.68      | -2.54 $\pm$ 0.63                    | No   | <sup>12</sup> CO <sub>2</sub> Ice, CH <sub>4</sub> ,               |
|                                   |                                  |  | Trailing   | 2.59 $\pm$ 0.34       | 5.69 $\pm$ 0.50                     | Yes  | Hydrocarbons   |
| 4.02 $\mu\text{m}$                | 4.021                            | 3.954–4.109                                | Leading    | 3.80 $\pm$ 0.31       | 35.47 $\pm$ 1.17                    | Yes  | <sup>12</sup> CO <sub>2</sub> Ice, CO <sub>3</sub>                 |
|                                   |                                  |  | Trailing   | 7.30 $\pm$ 0.66       | 65.38 $\pm$ 1.14                    | Yes  |  |
| <sup>c</sup> 4.15 $\mu\text{m}$   | <sup>L</sup> 4.147               | 4.117–4.187                                | Leading    | 7.33 $\pm$ 0.48       | 35.90 $\pm$ 0.86                    | Yes  | <sup>12</sup> CO <sub>2</sub> Ice, O-D                             |
|                                   | <sup>T</sup> 4.150               | 4.117–4.178                                | Trailing   | 9.50 $\pm$ 0.77       | 35.73 $\pm$ 0.67                    | Yes  |  |
| <sup>a,b</sup> 4.20 $\mu\text{m}$ | 4.202                            | 4.152–4.276                                | Leading    | 38.47 $\pm$ 0.83      | <sup>b</sup> 193.14 $\pm$ 1.61      | Yes  | <sup>12</sup> CO <sub>2</sub> Ice                                  |
|                                   |                                  |  | Trailing   | 126.13 $\pm$ 1.30     | 743.91 $\pm$ 2.19                   | Yes  |  |
| <sup>a,b</sup> 4.25 $\mu\text{m}$ | 4.252                            | 4.152–4.276                                | Leading    | 15.64 $\pm$ 0.85      | 193.14 $\pm$ 1.61                   | Yes  | <sup>12</sup> CO <sub>2</sub> Ice                                  |
|                                   |                                  |  | Trailing   | 82.42 $\pm$ 1.10      | 743.91 $\pm$ 2.19                   | Yes  |  |
| <sup>c</sup> 4.27 $\mu\text{m}$   | 4.273                            | 4.257–4.303                                | Leading    | 25.86 $\pm$ 1.21      | 43.45 $\pm$ 0.91                    | Yes  | <sup>12</sup> CO <sub>2</sub> Ice                                  |
|                                   |                                  |  | Trailing   | 41.24 $\pm$ 0.79      | 89.45 $\pm$ 0.79                    | Yes  |  |
| <sup>d</sup> 4.30 $\mu\text{m}$   | 4.298                            | 4.292–4.302                                | Leading    | 3.22 $\pm$ 1.43       | 1.35 $\pm$ 0.52                     | No   | <sup>16</sup> O <sup>12</sup> C <sup>18</sup> O Ice,               |
|                                   |                                  |  | Trailing   | 4.13 $\pm$ 0.87       | 1.59 $\pm$ 0.34                     | Yes  | amorphous CO <sub>2</sub>  |
| 4.38 $\mu\text{m}$                | 4.379                            | 4.365–4.391                                | Leading    | 7.82 $\pm$ 0.93       | 10.81 $\pm$ 0.68                    | Yes  | <sup>13</sup> CO <sub>2</sub> Ice                                  |
|                                   |                                  |  | Trailing   | 11.12 $\pm$ 1.04      | 16.19 $\pm$ 0.61                    | Yes  |  |
| 4.41 $\mu\text{m}$                | <sup>L</sup> 4.403               | 4.395–4.423                                | Leading    | 2.96 $\pm$ 0.88       | 3.20 $\pm$ 0.56                     | Yes  | <sup>16</sup> O <sup>13</sup> C <sup>18</sup> O Ice,               |
|                                   | <sup>T</sup> 4.412               | 4.393–4.429                                | Trailing   | 5.26 $\pm$ 1.13       | 8.38 $\pm$ 0.71                     | Yes  | C <sub>X</sub> O <sub>2</sub> , Nitriles                           |
| 4.47 $\mu\text{m}$                | 4.465                            | 4.430–4.495                                | Leading    | 2.66 $\pm$ 0.86       | 10.22 $\pm$ 1.05                    | Yes  | <sup>12</sup> CO <sub>2</sub> Ice, C <sub>X</sub> O <sub>2</sub> , |
|                                   |                                  |  | Trailing   | 6.11 $\pm$ 0.63       | 27.06 $\pm$ 1.04                    | Yes  | Nitriles   |
| 4.59 $\mu\text{m}$                | 4.593                            | 4.552–4.639                                | Leading    | 1.53 $\pm$ 0.60       | 6.08 $\pm$ 1.24                     | No   | <sup>12</sup> CO <sub>2</sub> Ice, OCN <sup>-</sup>                |
|                                   |                                  |  | Trailing   | 2.50 $\pm$ 0.73       | 14.90 $\pm$ 1.02                    | Yes  |  |
| 4.67 $\mu\text{m}$                | 4.675                            | 4.640–4.706                                | Leading    | 6.60 $\pm$ 1.09       | 11.64 $\pm$ 1.03                    | Yes  | <sup>12</sup> CO Ice   |
|                                   |                                  |  | Trailing   | 23.29 $\pm$ 0.76      | 63.06 $\pm$ 0.93                    | Yes  |  |
| 4.78 $\mu\text{m}$                | 4.780                            | 4.764–4.795                                | Leading    | 1.70 $\pm$ 0.65       | 0.35 $\pm$ 0.57                     | No   | <sup>13</sup> CO Ice, HCN  |
|                                   |                                  |  | Trailing   | 2.42 $\pm$ 0.25       | 4.17 $\pm$ 0.78                     | Yes  |  |
| 4.90 $\mu\text{m}$                | 4.898                            | 4.845–4.927                                | Leading    | 4.59 $\pm$ 0.76       | 11.57 $\pm$ 1.30                    | Yes  | <sup>12</sup> CO <sub>2</sub> Ice,                                 |
|                                   |                                  |  | Trailing   | 20.29 $\pm$ 0.96      | 64.77 $\pm$ 1.06                    | Yes  | CO <sub>3</sub>  |

**Notes.** L = Leading, T = Trailing. In the last column, confirmed constituents are shown in bold, and suggested constituents are italicized.

<sup>a</sup> Spectral features are peaks measured above the continuum.

<sup>b</sup> Band areas for the 4.20 and 4.25  $\mu\text{m}$  features are convolved, and we report the same band area for both peaks.

<sup>c</sup> The 4.15  $\mu\text{m}$  and 4.27  $\mu\text{m}$  features overlap the wavelength range of the 4.20  $\mu\text{m}$  and 4.25  $\mu\text{m}$  scattering peaks, and the reported measurements for these features (and their hemispherical asymmetries) are provided for completeness but are likely inaccurate.

<sup>d</sup> The 4.30  $\mu\text{m}$  feature is partly embedded in the long-wavelength wing of the 4.27  $\mu\text{m}$  feature.

Ariel's leading and trailing sides also exhibit prominent absorption features near 4.90  $\mu\text{m}$ , which corresponds to a biphonon + phonon combination mode, resulting from collective vibrations across a CO<sub>2</sub> ice lattice (Bini et al. 1991). Radiolytic carbon trioxide (CO<sub>3</sub>) may provide minor contributions to the 4.90  $\mu\text{m}$  feature (Figure A2). Another absorption band centered near 4.38  $\mu\text{m}$  is consistent with the  $\nu_3$  mode of <sup>13</sup>CO<sub>2</sub> ice. Ariel's large 4.25  $\mu\text{m}$  scattering peak coincides with the wavelength range where the extinction coefficient for CO<sub>2</sub>,  $k$ , is >1 and the refractive index,  $n$ , is <1 (Gerakines & Hudson 2020; Figure A3), suggesting that it is the largest CO<sub>2</sub> ice Fresnel peak yet observed on an icy body. For comparison, JWST revealed a much smaller CO<sub>2</sub> Fresnel

peak on Charon, shifted to  $\sim$ 4.265  $\mu\text{m}$  (Protopapa et al. 2023, 2024).

We calculated that 26.7% of Ariel's disk is sampled by both the leading and trailing hemisphere observations (Holler et al. 2016), with most of this overlap (18.7%) at  $>45^\circ$  north, where CO<sub>2</sub> is likely depleted (Grundy et al. 2006; Sori et al. 2017; Steckloff et al. 2022; Menten et al. 2023). We also measured a suite of less prominent absorption bands that may result from CO<sub>2</sub>, C<sub>X</sub>O<sub>2</sub>, carbonates, and nitriles (Appendix A.7), centered near 3.33, 4.02, 4.15, 4.30, 4.41, 4.47, and 4.59  $\mu\text{m}$  (Figures 2 and A4). Other tentative features that may result from CO<sub>2</sub> ice, but are too subtle to reliably measure, are centered near 3.01, 4.84, and 4.93  $\mu\text{m}$  (Figures 2, 4, and A4).

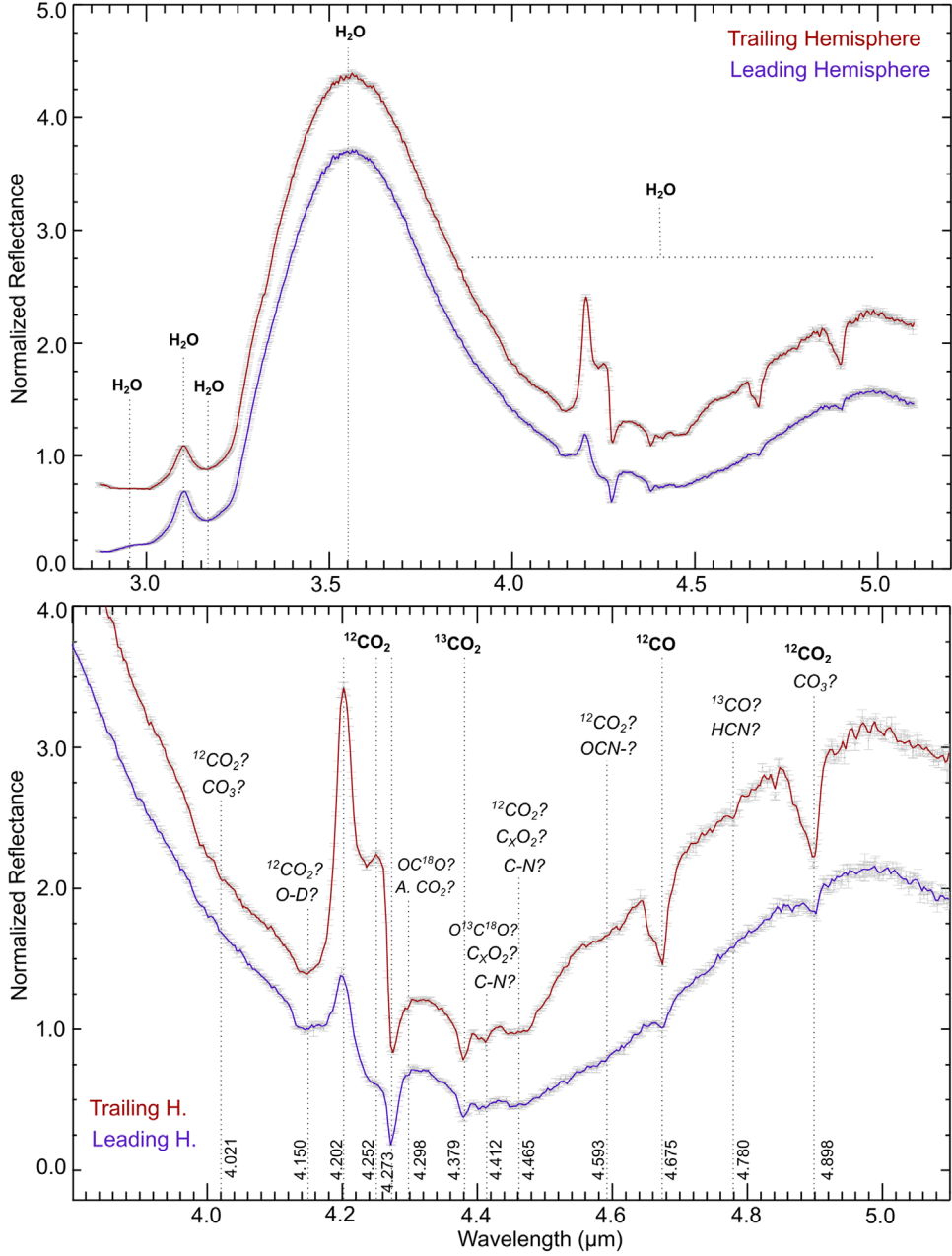


**Figure 1.** Top: NIRSpec IFU (G395M/F290LP) reflectance spectra and  $1\sigma$  uncertainties for Ariel’s leading (purple) and trailing (red) hemispheres, vertically offset for clarity and normalized to 1 at  $4.145 \mu\text{m}$ . Bottom: close-up of the same spectra, focusing on the  $3.8\text{--}5.1 \mu\text{m}$  wavelength region. Confirmed absorption bands and scattering peaks associated with H<sub>2</sub>O ice, CO<sub>2</sub> ice, and CO ice are shown in bold, whereas suggested constituents are italicized and followed by a question mark. Amorphous CO<sub>2</sub> is abbreviated to “A. CO<sub>2</sub>.” The central wavelengths ( $\mu\text{m}$ ) for the identified features are listed vertically along each dotted line and in Table 1.

**CO Ice:** The NIRSpec spectra show a prominent absorption feature near  $4.67 \mu\text{m}$  that is consistent with the  $\nu_3$  mode of <sup>12</sup>CO ice (e.g., Sandford et al. 1988; Bennett et al. 2010b), observed on a wide variety of trans-Neptunian objects (TNOs) and Centaurs by NIRSpec (e.g., Brown & Fraser 2023; Licandro et al. 2023; Emery et al. 2024; de Pra et al. 2024; Souza-Feliciano et al. 2024). CO ice should sublime rapidly at Ariel’s peak surface temperatures (80–90 K), and it is probably replenished on short timescales and perhaps complexed with a less volatile component, such as CO<sub>2</sub> (e.g., Sandford et al. 1988). Furthermore, Ariel’s  $4.67 \mu\text{m}$  feature exhibits flanking sidebands that are absent from pure CO ice (Figure 3, Section 3.3). A subtle feature near  $4.78 \mu\text{m}$  on Ariel’s trailing hemisphere likely results from <sup>13</sup>CO (see Appendix A.7 for

other interpretations). We also report <sup>13</sup>CO/<sup>12</sup>CO isotopic ratios (Appendix A.9) and modeling of possible <sup>13</sup>C enrichment (Appendix A.10).

**H<sub>2</sub>O Ice:** The spectral signature of H<sub>2</sub>O ice is apparent on both sides of Ariel, with clear evidence for the strong  $3.0 \mu\text{m}$   $\nu_3$  mode, the  $3.1 \mu\text{m}$  Fresnel peak indicative of crystalline H<sub>2</sub>O ice, the  $3.6 \mu\text{m}$  H<sub>2</sub>O ice continuum peak, and a broad  $4.5 \mu\text{m}$   $\nu_2 + \nu_K$  combination mode (Figure 1; Mastrapa et al. 2009 and references therein).

**What about NH<sub>3</sub>, Hydrocarbons, and H<sub>2</sub>O<sub>2</sub>?** The NIRSpec spectra do not display evidence for the  $2.96 \mu\text{m}$   $\nu_3$  mode indicative of NH-bearing species, nor other features associated with NH<sub>3</sub> or NH<sub>4</sub>. NH-bearing features between 2.9 and  $3.2 \mu\text{m}$  are also apparently absent from Charon (Protopapa

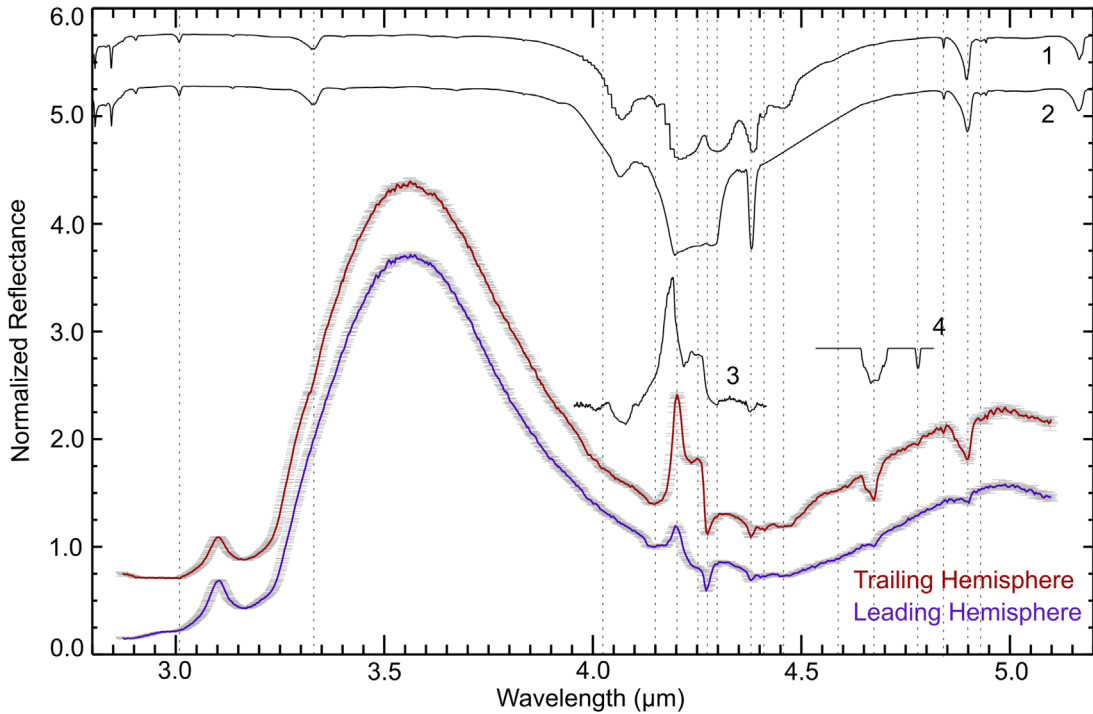


**Figure 2.** Comparison between Ariel’s leading (purple) and trailing (red) hemisphere spectra (vertically offset for clarity, normalized to unity at  $4.145\ \mu\text{m}$ ) and  $1\sigma$  uncertainties, along with synthetic spectra of crystalline  $\text{CO}_2$  ice (1–3) and CO ice (4). These synthetic spectra were generated using  $\text{CO}_2$  grain diameters and optical constants from: model 1,  $10\ \mu\text{m}$ , Hansen (1997); model 2,  $10\ \mu\text{m}$ , Quirico & Schmitt (1997a, 1997b); model 3,  $50\ \mu\text{m}$ , Gerakines & Hudson (2020); model 4,  $10\ \mu\text{m}$ , Robert Brown (private communication). Models 1 and 2 were scaled to the depth of the  $4.90\ \mu\text{m}$  band on Ariel’s trailing side, Model 3 was scaled to the height of the  $4.20\ \mu\text{m}$  scattering peak on Ariel’s trailing side, and Model 4 was scaled to the depth of the  $4.67\ \mu\text{m}$  band on Ariel’s trailing side. All four models are offset vertically for clarity. The central wavelength of measured features (Table 1) and possible features near  $3.01$ ,  $4.84$ , and  $4.93\ \mu\text{m}$  are indicated by dotted lines.

et al. 2023, 2024), which exhibits a prominent  $2.2\ \mu\text{m}$  band long attributed to NH-bearing compounds (e.g., Brown & Calvin 2000; Buie & Grundy 2000; Grundy et al. 2016; Cook et al. 2018, 2023; Protopapa et al. 2020). Thus, NH-bearing species may contribute to Ariel’s  $2.2\ \mu\text{m}$  band but are obscured by  $\text{H}_2\text{O}$  ice absorption in the  $3\ \mu\text{m}$  region sampled by G395M data. We also find no reliable evidence for C–H stretching modes exhibited by hydrocarbons between  $3.2$  and  $3.5\ \mu\text{m}$ , nor any evidence for a prominent  $\text{H}_2\text{O}_2$  combination mode ( $\nu_1 + \nu_6$ ) near  $3.51\ \mu\text{m}$  (Figure A5; Bain & Giguère 1955).

### 3.2. Band Parameter Measurements

We measured seven confirmed features in both spectra and another eight likely features on Ariel’s trailing hemisphere, four of which are also on Ariel’s leading side ( $>3\sigma$  detection; Table 1). The  $3.1\ \mu\text{m}$   $\text{H}_2\text{O}$  Fresnel peak is significantly stronger on Ariel’s leading side. In contrast, all of the features that are definitively associated with  $\text{CO}_2$  and CO ice are stronger on Ariel’s trailing hemisphere. The distributions of  $\text{H}_2\text{O}$  and  $\text{CO}_2$  are consistent with the hemispherical trends established in ground-based studies (e.g., Grundy et al. 2003; Cartwright et al. 2022). The features centered near  $4.02$ ,  $4.41$ , and  $4.47\ \mu\text{m}$  are significantly stronger on Ariel’s trailing side ( $>3\sigma$  difference). The  $3.33$ ,  $4.30$ ,  $4.59$ , and  $4.78\ \mu\text{m}$  bands are only reliably detected on Ariel’s trailing hemisphere ( $>3\sigma$  detection; Table 1).

### 3.3. Synthetic and Laboratory Spectra of $\text{CO}_2$ and CO Ice

We compared the Ariel data to synthetic spectra of crystalline  $\text{CO}_2$  ice (models 1–3) and CO ice (model 4), shown in Figure 2. These comparisons highlight the large

number of subtle features that can be expressed by  $\text{CO}_2$  ice (models 1 and 2), many of which appear to be present on Ariel (Table 1). Furthermore, Ariel’s  $\text{CO}_2$  scattering peaks can be approximated by a layer of large  $\text{CO}_2$  grains ( $\geq 50\ \mu\text{m}$  diameters; model 3). The synthetic spectrum of CO ice matches the central wavelength positions of Ariel’s  $4.67$  and  $4.78\ \mu\text{m}$  features (model 4), confirming the presence of this molecule and possibly confirming its heavy-carbon isotopologue.

Figure 3(a) shows laboratory data of CO and  $\text{CO}_2$  mixtures, whereas Figure 3(b) shows CO generated in proton-irradiated  $\text{CO}_2$  ice films containing CO and  $\text{O}_2$ , with trace amounts of  $\text{CO}_3$  and  $\text{O}_3$  (Raut & Baragiola 2013). The pure CO sample exhibits a narrow sideband that likely results from a longitudinal optical (LO) phonon mode caused by collective oscillations within the ice’s structure. Similar LO modes have been reported for  $\text{CO}_2$  samples illuminated at oblique angles (Cooke et al. 2016). However, this  $4.658\ \mu\text{m}$  sideband exhibited by Ariel’s  $4.67\ \mu\text{m}$  feature is broader than pure CO and more similar to the sidebands exhibited by mixed CO +  $\text{CO}_2$  samples, consistent with prior work (Sandford et al. 1988). We speculate that these sidebands result from CO dimers and trimers with vibrational frequencies distinct from monomeric CO.

The  $\nu_3$  mode in the proton-generated CO sample we analyzed is centered at shorter wavelengths ( $\sim 4.668\ \mu\text{m}$ ) than Ariel’s  $4.67\ \mu\text{m}$  band ( $4.675\ \mu\text{m}$ ) and does not match its sidebands (Figure 3). Similarly, another study that generated CO via electron irradiation of  $\text{CO}_2$  (20–50 K) measured a band center of  $4.671\ \mu\text{m}$  for its  $\nu_3$  mode (Mifsud et al. 2022), slightly offset from Ariel’s  $4.67\ \mu\text{m}$  band. Thus, radiolytic CO may not be the primary contributor to CO on Ariel. Alternatively, ice annealing processes and CO diffusion to lower energy sites in

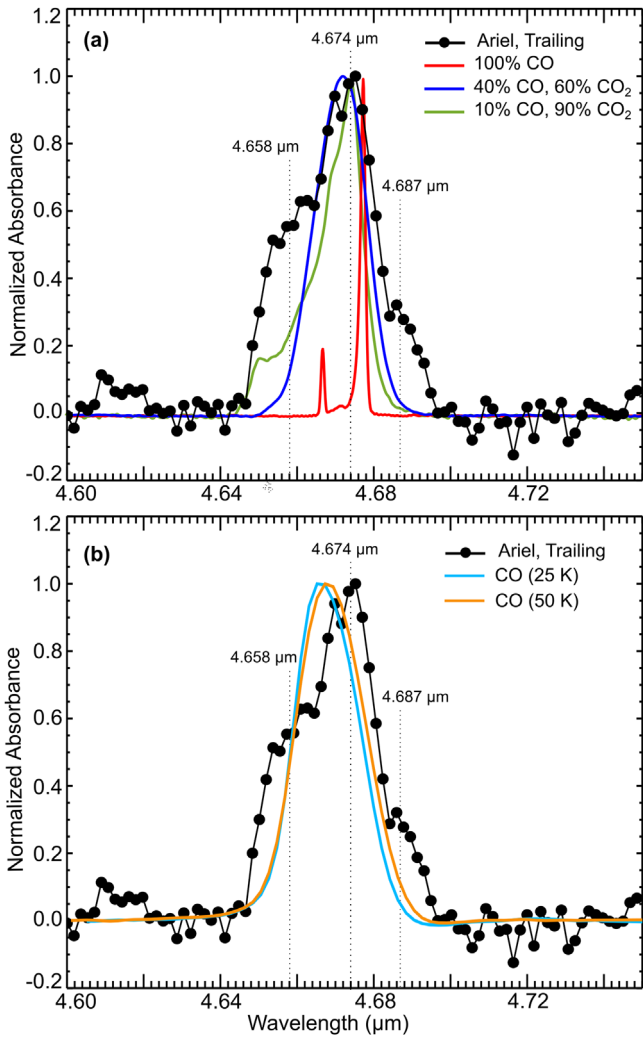


**Figure 3.** (a) Comparison between a continuum-subtracted version of the 4.67  $\mu\text{m}$  absorption band on Ariel’s trailing hemisphere (black) and laboratory absorbance spectra of pure CO ice and CO + CO<sub>2</sub> ice mixtures measured in the Astrophysical Material Laboratory at temperatures between 20 and 30 K, with the CO feature persisting at temperatures up to 80 K in the mixed CO + CO<sub>2</sub> samples (Tegler et al. 2024; Grundy et al. 2024a). Pure CO<sub>2</sub> ice is essentially featureless in this wavelength range and omitted for clarity. The CO<sub>2</sub>:CO mixture (9:1, green, centered near 4.674  $\mu\text{m}$ ) provides a good match to the central wavelength of Ariel’s 4.67  $\mu\text{m}$  band, whereas mixtures with comparable amounts of CO<sub>2</sub> and CO (6:4, blue, centered near 4.672  $\mu\text{m}$ ) provide less ideal matches. Pure CO ice (red, 4.677  $\mu\text{m}$ ) is much narrower, offset to longer wavelengths, and exhibits a narrow sideband (4.667  $\mu\text{m}$ ), likely resulting from a longitudinal optical phonon mode, which does not match the broad short-wavelength sideband of Ariel’s 4.67  $\mu\text{m}$  band. Neither the pure CO nor CO + CO<sub>2</sub> mixtures are able to match Ariel’s long-wavelength sideband centered near 4.69  $\mu\text{m}$ . (b) Comparison between a continuum-subtracted version of the 4.67  $\mu\text{m}$  band on Ariel’s trailing hemisphere (black) and laboratory spectra of a sample dominated by CO ice generated via irradiation of a CO<sub>2</sub> thin film with 100 KeV H<sup>+</sup> protons at 25 K (light blue) and 50 K (orange), shown in optical depth units ( $-\ln(R/R_0)$ , where  $R$  is the reflectance of the film and gold substrate and  $R_0$  is the reflectance of the bare gold substrate; Raut & Baragiola 2013). All spectra are normalized to 1 at their maxima. The radiolytic CO features do not provide good matches to the central position, width, or sidebands of Ariel’s 4.67  $\mu\text{m}$  band.

the surrounding CO<sub>2</sub> lattice might obscure the signature of radiolytic CO over time, making interpretation more difficult.

The other sideband ( $\sim 4.687 \mu\text{m}$ ) expressed by Ariel’s 4.67  $\mu\text{m}$  feature is absent from pure CO ice, CO + CO<sub>2</sub> mixtures, and radiolytic CO, suggesting mixing with other species, including H<sub>2</sub>O (Sandford et al. 1988), CO clathrates

(Dartois et al. 2011), or perhaps carbonates. Comparison between these Ariel data and laboratory spectra of irradiated carbonates and other carbon oxides could test our inference, based on Figure 3, that CO may be (partially) native to Ariel. Similarly, new optical constants for CO + CO<sub>2</sub> mixtures and CO<sub>2</sub> mixed with other carbon oxides are likely required to better understand Ariel’s spectral properties.

## 4. Discussion

### 4.1. Concentrated Deposits of CO<sub>2</sub> Ice

The results presented here and in prior studies (Grundy et al. 2003, 2006; Cartwright et al. 2015, 2020b) indicate that CO<sub>2</sub> on Ariel has remarkably similar spectral properties to crystalline CO<sub>2</sub> ice measured in the laboratory (i.e., CO<sub>2</sub> molecules primarily bonded to each other in a long-range order). Comparison to synthetic spectra of crystalline CO<sub>2</sub> ice (Figure 2) highlights that Ariel exhibits many subtle CO<sub>2</sub> features outside of the strong  $\nu_3$  mode. Specifically, the 3.33  $\mu\text{m}$  and 4.90  $\mu\text{m}$  bands and other possible features near 3.01, 3.33, 4.84, 4.90, and 4.93  $\mu\text{m}$  on Ariel’s trailing hemisphere do not appear on many other objects where CO<sub>2</sub> has been detected by JWST/NIRSpec (e.g., Brown & Fraser 2023; Pinto et al. 2023; Villanueva et al. 2023; Bockelee-Morvan et al. 2024; Cartwright et al. 2024; de Pra et al. 2024; Emery et al. 2024; Protopapa et al. 2024; Wong et al. 2024; TNO examples provided in Figure A6), with the exception of Triton (Wong et al. 2023). Consequently, Ariel’s surface exhibits some of the most CO<sub>2</sub>-rich deposits in the solar system.

To estimate the thickness of Ariel’s CO<sub>2</sub> ice deposits, we calculated the  $e$ -folding depths ( $1/\alpha$ , where  $\alpha$  is the absorption coefficient) for near-infrared (NIR) photons propagating through a slab of CO<sub>2</sub> ice, which is essentially an application of the Beer–Lambert absorption law. To account for scattering off grain boundaries, we calculated the mean optical path length, MOPL =  $-1/(\alpha^* \ln(R))$ , where  $R$  is the reflectance (Clark & Roush 1984), using synthetic spectra composed of CO<sub>2</sub> ice grains (1, 10, and 100  $\mu\text{m}$  diameters). The results of these two approaches indicate that photons spanning the wavelength range of the CO<sub>2</sub>  $\nu_3$  band (4.1–4.4  $\mu\text{m}$ ) can travel 0.0001–0.1 mm into slabs of CO<sub>2</sub> ice or deposits dominated by CO<sub>2</sub> grains before being absorbed (Figure 4). In contrast, photons penetrate  $>0.3$  mm in the wavelength range of the 4.90  $\mu\text{m}$  band,  $\sim 4$  mm in the wavelength ranges of the 3.33 and 4.84  $\mu\text{m}$  bands, and upward of 10 mm in the wavelength ranges of the possible 3.01 and 4.93  $\mu\text{m}$  features (Figure 4). The penetration depth estimates reported here are broadly consistent with prior estimates made on weak CO<sub>2</sub> features between 1.5–1.7  $\mu\text{m}$  (4–30 mm depths) and 1.9–2.1  $\mu\text{m}$  (0.07–0.4 mm depths) detected on Ariel (Cartwright et al. 2015, 2022). Additionally, these estimates are consistent with laboratory measurements of CO<sub>2</sub> ice optical constants, which used thin films (0.25–3  $\mu\text{m}$  thick) to avoid saturation while measuring the  $\nu_3$  mode (Gerakines & Hudson 2020) and samples  $>10$  mm thick to measure weaker CO<sub>2</sub> features (Hansen 1997, 2005).

As an additional test, we generated synthetic spectra composed of CO<sub>2</sub> in areal and particulate mixtures with CO, H<sub>2</sub>O, and amorphous carbon. We found that the CO<sub>2</sub>  $\nu_3$  mode is present in all areal and particulate mixtures, and weaker CO<sub>2</sub> features are present in areal mixtures (see Appendix A.2 for model details). In contrast, weak features near 3.01, 3.33, 4.84, and 4.93  $\mu\text{m}$  are not present in any of the particulate mixture

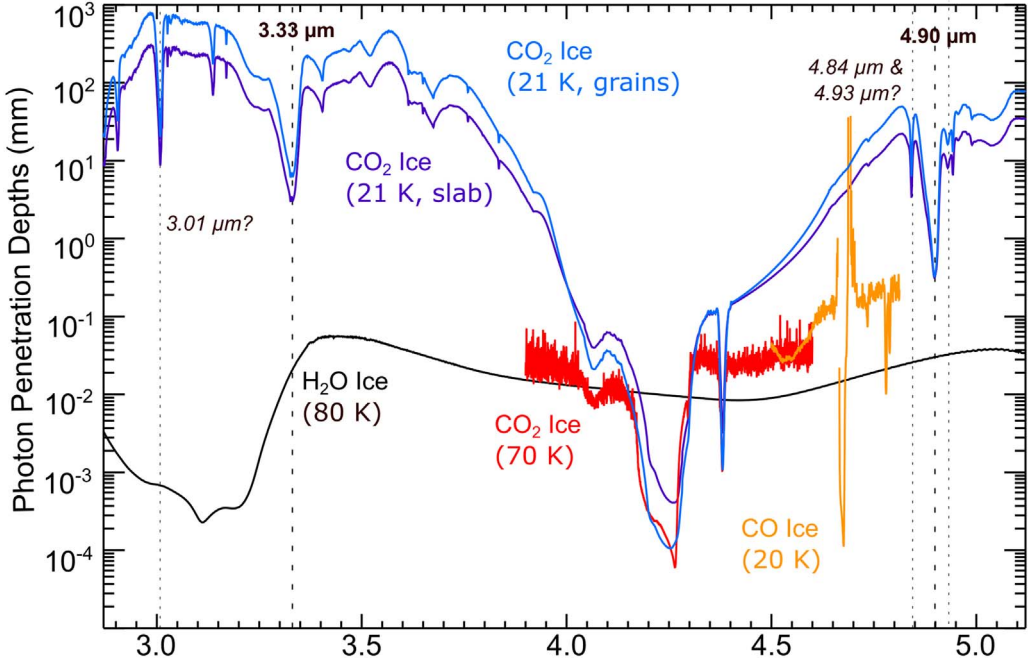


**Figure 4.** The  $e$ -folding photon penetration depths into a slab of  $\text{CO}_2$  ice (red: Gerakines & Hudson 2020; purple: Quirico & Schmitt 1997a, 1997b), CO ice (orange; Gerakines et al. 2023), and  $\text{H}_2\text{O}$  ice (black; Mastrapa et al. 2009), and MOPLs for photons into a layer of  $\text{CO}_2$  ice grains with  $1 \mu\text{m}$  diameters (blue). The MOPLs for photons into layers composed of 10 and  $100 \mu\text{m}$  diameter  $\text{CO}_2$  ice grains are intermediate between the blue and purple lines. The black dashed lines highlight the band centers for Ariel's 3.33 and 4.90  $\mu\text{m}$  bands, and the gray dashed lines highlight other subtle  $\text{CO}_2$  ice features that may be present in the spectrum of Ariel's trailing hemisphere (centered near 3.01, 4.84, and 4.93  $\mu\text{m}$ ). This plot shows that only the strong  $\nu_3$  modes for  $^{12}\text{CO}_2$ ,  $^{13}\text{CO}_2$ ,  $^{12}\text{CO}$ , and  $^{13}\text{CO}$  should be exhibited by Ariel, if carbon oxides are well mixed with  $\text{H}_2\text{O}$  on its surface. The presence of weaker  $\text{CO}_2$  ice features supports the presence of concentrated  $\text{CO}_2$  ice deposits exposed on Ariel's surface (likely mixed with small amounts of CO and perhaps other carbon oxides).

models, while the 4.90  $\mu\text{m}$  band is present in particulate mixture models that include  $\geq 40\%$   $\text{CO}_2$  (Figure A1). These results support the hypothesis that  $\text{CO}_2$  ice on Ariel's surface is segregated from  $\text{H}_2\text{O}$  ice. Whether these  $\text{CO}_2$ -dominated deposits are spatially associated with specific geologic landforms, or are more regionally dispersed, cannot be determined with these disk-integrated spectra.

#### 4.2. Radiolytic Production and Seasonal Migration of CO and $\text{CO}_2$

At winter temperatures of 20–30 K,  $\text{CO}_2$  and CO ices are stable and likely form a winter cap. Once exposed to sunlight in spring,  $\text{CO}_2$  and CO should start to sublimate and migrate to cold traps near the new winter pole or leave the surface environment via Jeans escape, in particular for the more volatile CO. Seasonal migration of  $\text{CO}_2$  molecules could lead to the formation of a transient layer of pure  $\text{CO}_2$  frost grains that is predicted to be up to 2.4 mm thick (Steckloff et al. 2022). Scattering within such a thick layer of seasonally mobile  $\text{CO}_2$  grains might contribute to Ariel's large 4.20 and 4.25  $\mu\text{m}$  scattering peaks. Furthermore, the JWST/NIRSpec results presented here indicate that  $\text{CO}_2$  ice deposits could be upward of 10 mm thick on Ariel's trailing hemisphere (Section 4.1), raising the possibility that  $\text{CO}_2$  deposits on its trailing side are sufficiently thick to be partly resistant to seasonal migration. On Ariel's leading hemisphere,  $\text{CO}_2$  deposits may be only  $\sim 0.3$  mm thick (Figure 4), suggesting that  $\text{CO}_2$  on its leading side may primarily result from sublimation and transport from its trailing hemisphere.

One way to explain how Ariel retains CO is if it forms at depth via radiolytic decomposition of thick  $\text{CO}_2$  deposits. Measurements made by Voyager 2 indicate that heavy ions are

largely absent from Uranus's magnetosphere (Ness et al. 1986), suggesting that high-energy electrons and protons could be the primary drivers of radiolytic processes. Energy deposition by protons and heavy ions is mostly limited to the top 0.01 mm of icy regoliths (e.g., Delitsky & Lane 1998), but energetic electrons ( $\sim 1$  MeV) can penetrate centimeter-scale depths into ices (e.g., Nordheim et al. 2017). CO molecules generated at depth would be stable at Ariel's winter pole before diffusing out of its regolith once exposed to sunlight, possibly being retained long enough to be detected. Alternatively, geologic sources of native CO could help replenish CO ice on Ariel's surface (Figure 3, Section 3.3).

#### 4.3. Possible Internally Derived Materials

The 2.2  $\mu\text{m}$  bands detected in ground-based observations of the Uranian moons have been attributed to potentially internally derived deposits rich in  $\text{NH}_3$  hydrates and  $\text{NH}_3$  ice, carbonates, phyllosilicates, and/or organics (e.g., Cartwright et al. 2020a, 2023; DeColibus et al. 2023). Although we did not detect evidence of NH-bearing species, phyllosilicates, or hydrocarbons in the G395M data, Ariel's 4.02  $\mu\text{m}$  feature could result from a  $\nu_1 + \nu_3$  combination mode expressed by  $\text{CO}_3$  in carbonate minerals (Hexter 1958; Bishop et al. 2021), similar to Callisto's 4.02  $\mu\text{m}$  band (Johnson et al. 2004; Cartwright et al. 2024). Laboratory experiments show that although radiolytic  $\text{CO}_3$  exhibits a 4.89  $\mu\text{m}$  feature (Figure A2; Raut & Baragiola 2013), a complementary 4  $\mu\text{m}$   $\text{CO}_3$  band was not observed in these irradiation experiments. Similarly, carbonic acid ( $\text{H}_2\text{CO}_3$ ), generated via irradiation of  $\text{H}_2\text{O}$  and  $\text{CO}_2$  mixtures at cryogenic temperatures ( $< 100$  K), exhibits a broad absorption band between 3.8 and 3.9  $\mu\text{m}$  (e.g., Moore & Khanna 1991; Hage et al. 1998; Gerakines et al. 2000), but it is

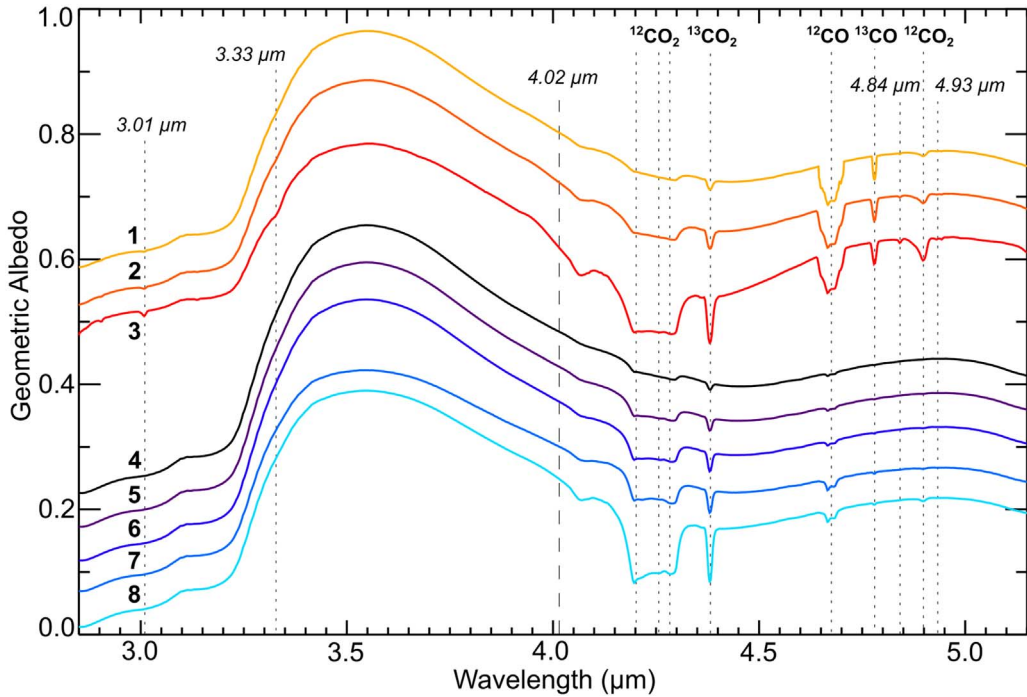


**Figure A1.** Synthetic spectra (Appendix A.2) composed of areal (models 1–3) and particulate (models 4–8) mixtures, offset vertically for clarity. These spectral models include crystalline H<sub>2</sub>O ice (Mastrapa et al. 2009), crystalline CO<sub>2</sub> ice (Quirico & Schmitt 1997a, 1997b), crystalline CO ice (Robert Brown, private communication), and amorphous carbon (Rouleau & Martin 1991), with grain diameters of 2, 10, 10, and 1 μm, respectively. Each model includes 10% CO ice and 0.5% amorphous carbon mixed with (1) 84.5% H<sub>2</sub>O ice and 5% CO<sub>2</sub> ice, (2) 79.5% H<sub>2</sub>O ice and 10% CO<sub>2</sub> ice, (3) 64.5% H<sub>2</sub>O ice and 25% CO<sub>2</sub> ice, (4) 64.5% H<sub>2</sub>O ice and 25% CO<sub>2</sub> ice, (5) 49.5% H<sub>2</sub>O ice and 40% CO<sub>2</sub> ice, (6) 39.5% H<sub>2</sub>O ice and 50% CO<sub>2</sub> ice, (7) 14.5% H<sub>2</sub>O ice and 75% CO<sub>2</sub> ice, and (8) 14.5% H<sub>2</sub>O ice and 75% CO<sub>2</sub> ice. Model 7 includes 25% CO<sub>2</sub> (Quirico & Schmitt 1997a; 10 μm grains) and 50% CO<sub>2</sub> (Gerakines & Hudson 2020; 100 μm grains). These models demonstrate that the Ariel features between 4.19 and 4.30 μm and between 4.65 and 4.80 μm, which are associated with the  $\nu_3$  modes of CO<sub>2</sub> and CO ice, respectively, are exhibited by all eight models (dotted lines with bold text). In contrast, weak CO<sub>2</sub> features tentatively observed on Ariel, near 3.01, 3.33, 4.84, and 4.93 μm (dotted lines, italicized text), are only exhibited by areal mixtures that include  $\geq 10\%$  CO<sub>2</sub> (models 2–3) and are not observed in any of the particulate mixtures (25%–75% CO<sub>2</sub> ice; models 4–8). The 4.90 μm band is expressed by all areal mixtures (5%–25% CO<sub>2</sub>, models 1–3) and particulate mixtures with  $\geq 40\%$  CO<sub>2</sub> (models 5–8). The presence of weak CO<sub>2</sub> ice features in the areal mixtures and their absence from the particulate models demonstrate that concentrated deposits of pure CO<sub>2</sub> on Ariel’s surface are required for these features to be expressed (Section 4.1). None of the areal or particulate mixtures exhibit a  $\sim 4\text{ }\mu\text{m}$  feature, suggesting that carbonates, or another component, are more likely to contribute to Ariel’s 4.02 μm band compared to CO<sub>2</sub> ice (dashed line, italicized text).

uncertain what processes might cause this feature to shift to longer wavelengths, matching Ariel’s 4.02 μm band. Radiolytically-formed, CO<sub>3</sub>-bearing species are therefore unlikely to contribute to Ariel’s 4.02 μm band, and nonradiolytic, native carbonates seem to be more likely to contribute.

A prior study suggested that Umbriel’s 2.2 μm band may result from thermonatrite (Na<sub>2</sub>CO<sub>3</sub> · H<sub>2</sub>O), possibly contributing to bright crater floor deposits (Cartwright et al. 2023), along with cold-trapped CO<sub>2</sub> ice (Sori et al. 2017). In this scenario, emplaced carbonates could serve as base material for radiolytic CO<sub>2</sub>, or perhaps endogenic CO<sub>2</sub> could be delivered from Ariel’s interior with carbonates, either at present or in the geologic past. Indeed, it is predicted that within deep oceans evolved from carbon-rich ices, a large fraction of CO<sub>2</sub> (several hundreds of mmol/(kg H<sub>2</sub>O)) may be in solution with bicarbonate (Castillo-Rogez et al. 2022). If CO<sub>2</sub> is outgassed from Ariel’s interior, then some of it should condense and contribute to the concentrated CO<sub>2</sub> ice deposits detected in JWST and ground-based data sets. Endogenic CO<sub>2</sub>, if mixed with liquid H<sub>2</sub>O and coexisting with bicarbonate, could indicate a mildly acidic ocean (pH  $\sim 6$ –8), favoring the surface precipitation of bicarbonate salts and potentially Mg or Ca carbonates at lower pH values (e.g., Glein et al. 2015; Tosi et al. 2024). Alternatively, radiolytic CO<sub>2</sub>, or native CO<sub>2</sub> sequestered in Ariel’s crust, would permit a more basic ocean

chemistry (pH  $> 9$ –10), supporting Na and NH<sub>4</sub> carbonate precipitation.

The presence of carbonates would have important implications for minerals possibly formed in an aqueous environment and for the habitability of Ariel’s interior, including the availability of phosphorus (Postberg et al. 2023), a key chemical component for life. Except for NH<sub>4</sub> carbonates, carbonate salts require environments where silicate minerals can interact with liquid H<sub>2</sub>O (Castillo-Rogez et al. 2022). Such formation environments may exist at rock–water interfaces in ocean world interiors such as Ceres, whose strong 4 μm band results from carbonates (e.g., Rivkin et al. 2006), including Na<sub>2</sub>CO<sub>3</sub> salts (e.g., De Sanctis et al. 2016; Carrozzo et al. 2018; Raponi et al. 2019), likely formed from the alteration of rock in contact with an ocean that included NH<sub>3</sub> (Castillo-Rogez et al. 2018). Similarly, Enceladus’s plume particles are dominated by H<sub>2</sub>O ice mixed with minor amounts of Na carbonates (Postberg et al. 2009) and Na phosphates (Postberg et al. 2023) that likely formed in its ocean.

If CO is internally derived and released during winter, it could persist on Ariel’s surface, condensing with CO<sub>2</sub>. To survive in Ariel’s interior, endogenic CO would need to be sequestered in its crust and unable to interact with liquid H<sub>2</sub>O, or else it would have oxidized to CO<sub>2</sub> or reduced to metastable organic compounds, such as formic acid/formate and perhaps CH<sub>4</sub> (Neveu et al. 2015; Glein & Waite 2018). CO trapped as

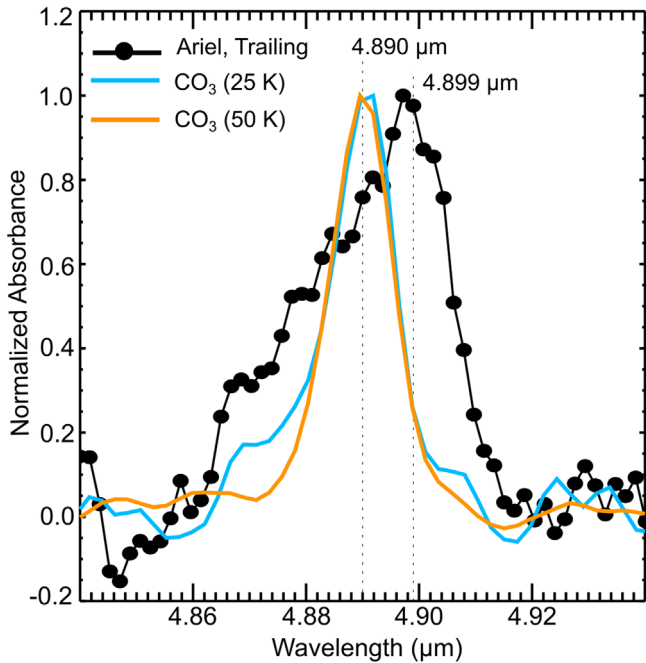


**Figure A2.** Comparison between a continuum-subtracted version of Ariel’s 4.90  $\mu\text{m}$  band on its trailing hemisphere and a 4.89  $\mu\text{m}$   $\text{CO}_3$  band generated via irradiation of  $\text{CO}_2$  ice thin film with 100 keV  $\text{H}^+$  protons, scaled in optical depth units ( $-\ln(R/R_0)$ , where  $R$  is the reflectance of the film and gold substrate and  $R_0$  is the reflectance of the bare gold substrate; Raut & Baragiola 2013). All spectra are normalized to 1 at their maxima. The offset between the  $\text{CO}_3$  features and Ariel’s 4.90  $\mu\text{m}$  band supports the interpretation that this feature results from collective oscillations across a crystalline  $\text{CO}_2$  ice lattice (Bini et al. 1991; Figure 2). It is possible that radiolytically produced  $\text{CO}_3$  contributes to the broad short-wavelength side of Ariel’s 4.90  $\mu\text{m}$  band. However, additionally experiments are required to determine whether this broadening of Ariel’s 4.90  $\mu\text{m}$  band results from mixing with  $\text{CO}_3$  or other variables such as the temperature of  $\text{CO}_2$  on Ariel.

guest molecules in clathrates, however, would be more resistant to these processes and might persist. CO clathrates exhibit a  $^{12}\text{CO}$   $\nu_3$  mode near 4.685  $\mu\text{m}$  (Dartois 2011), potentially matching a sideband on Ariel’s 4.67  $\mu\text{m}$  feature (Figure 3). Furthermore, the detection of CO in Enceladus’s plume material (e.g., Peter et al. 2024) demonstrates that CO can survive in warm icy satellite interiors.

## 5. Summary and Conclusions

We analyzed JWST/NIRSpec spectral observations collected over Ariel’s leading and trailing hemispheres, revealing the presence of crystalline  $\text{CO}_2$  ice and CO ice mixed with  $\text{CO}_2$ . We detected a suite of other spectral features that might result from carbonates,  $\text{C}_3\text{O}_2$ , and nitriles. The detected  $\text{CO}_2$  ice is likely concentrated in thick deposits, possibly mixed with a small amount of CO, but the physical state of these deposits and whether they are associated with geologic conduits to Ariel’s interior are difficult to determine with these disk-integrated spectra. Spatially resolved NIR spectra collected by an orbiter making close flybys of the Uranian moons are required to explore the spatial relationship between volatiles and geologic features and confirm whether some carbon oxides originate in Ariel’s interior (e.g., Beddingfield et al. 2020; Cartwright et al. 2021; Leonard et al. 2021; Cohen et al. 2022; National Academies of Sciences, Engineering, & Medicine 2023).

We found no compelling evidence for NH-bearing species, hydrocarbons, or  $\text{H}_2\text{O}_2$  in the G395M data, although NH-bearing species could be present but obscured by strong 3  $\mu\text{m}$   $\text{H}_2\text{O}$  ice absorption. The lack of hydrocarbon features suggests that amorphous carbon dominates the low albedo material that is well mixed with  $\text{H}_2\text{O}$  ice in the Uranian moons’ regoliths, possibly also mixed with some “amorphous silicates” (Cartwright et al. 2018). The apparent absence of  $\text{H}_2\text{O}_2$  suggests that the irradiation environment at Ariel may be fairly quiescent, or extensive  $\text{CO}_2$  deposits limit interactions between charged particles and underlying  $\text{H}_2\text{O}$  ice.

## Acknowledgments

This work is based on observations made with the NASA/ESA/CSA James Webb Space Telescope. The data were obtained from the Mikulski Archive for Space Telescopes at the Space Telescope Science Institute, which is operated by the Association of Universities for Research in Astronomy, Inc., under NASA contract NAS 5-03127 for JWST. These observations are associated with GO program 1786. Support for GO program 1786 was provided by NASA through a grant from the Space Telescope Science Institute, which is operated by the Association of Universities for Research in Astronomy, Inc., under NASA contract NAS 5-03127.

## Appendix

### A.1. Data and Methods: NIRSpec Observations

Data processing utilized the Science Calibration Pipeline v1.13.4 with CRDS context jwst\_1214.pmap to process raw *uncal* data into *s3d* spectral cubes for each of the four dithers (Bushouse et al. 2023). The pipeline was run using the default parameters and including the NSClean routine to remove the  $1/f$  pattern noise (Rauscher 2024). The spectral extraction used a “template PSF-fitting” routine. The wavelength grid was first computed using the *CRVAL3* and *CRDELT3* header keywords, with each wavelength corresponding to a specific slice in the data cube. An initial by-eye estimate was made for the centroid position of the target (Ariel is a point source given the 0.1 NIRSpec pixels). The background was then calculated as the median of all pixels  $>5$  pixels from the centroid and subtracted from all pixels in the slice. The “template PSF” was then calculated by taking the median of a moving 21-slice window. A  $9 \times 9$  pixel box was cut out around the centroid of the template PSF, normalized to unity within the box, and iteratively fit to the slice in the middle of the 21-slice window using the *scipy.optimize.minimize* function and the Nelder-Mead algorithm. The two fit parameters were the flux scaling factor and the background, which were used to construct the best-fit model. The 1D spectrum was constructed by extracting the flux within a 3.5-pixel-radius circular aperture, centered on the centroid in each slice. To remove the solar component, the four dithers were medianed and then divided by a median G395M spectrum of P330E, a well-established spectrophotometric calibration star (G0V,  $\text{Vmag}$   $13.028 \pm 0.004$ ; e.g., Bohlin & Landolt 2015). The individual P330E spectra were computed using the same template PSF-fitting routine described above. Uncertainties for the Ariel and P330E spectra were computed as the median absolute deviation within each wavelength bin, with the uncertainties propagated to the final P330E-divided spectra (Figure 1).

### A.2. Data and Methods: Radiative Transfer Modeling

The synthetic spectra reported in this study were generated by adopting Mie scattering theory (e.g., Bohren & Huffman 1983) to calculate the single scattering albedo ( $\bar{\omega}_0$ ) for each component using their real,  $n$ , and imaginary,  $k$ , parts of the complex refractive index, derived from laboratory experiments for crystalline CO<sub>2</sub> ice (150 K, Hansen 1997; 70 K, Gerakines & Hudson 2020; 21 K, Quirico & Schmitt 1997a, 1997b), CO ice (Robert Brown, private communication; 20 K, Gerakines et al. 2023), crystalline H<sub>2</sub>O ice (80 K; Mastrapa et al. 2009), and amorphous carbon (room temperature; Rouleau & Martin 1991). These  $\bar{\omega}_0$  values were then passed to Hapke equations that calculate geometric albedo as a function of wavelength (Hapke 2012). The program generates one-layer models of end-member species (like those shown in Figure 2) or particulate or areal mixtures of various components (Figure A1). Minor resonances in synthetic spectra generated using Mie-derived  $\bar{\omega}_0$  are addressed by calculating albedo using a range of grain sizes ( $\pm 10\%$  spread in diameters), which are then averaged at each wavelength step in the final model. Although Mie scattering theory only approximates the structure of planetary regoliths, it is widely used in radiative transfer models to simulate the surfaces of icy bodies. More details and caveats on this program and its prior application to simulate the spectral properties of the Uranian moons' surfaces are provided in, e.g., Cartwright et al. (2023).

### A.3. Results and Analyses: Comparison between Ariel's 4.90 $\mu\text{m}$ Band and Radiolytically Formed CO<sub>3</sub>

Here we report laboratory spectra of radiolytically generated CO<sub>3</sub> compared to Ariel's 4.90  $\mu\text{m}$  band (Figure A2).

### A.4. Results and Analyses: Ariel's CO<sub>2</sub> Scattering Peak Compared to the Indices of Refraction for CO<sub>2</sub>

Here we report an arbitrarily scaled NIRSpec spectrum of Ariel's trailing hemisphere compared to the indices of refraction for CO<sub>2</sub>, measured by Gerakines & Hudson (2020; Figure A3).

### A.5. Results and Analyses: Ariel Trailing/Ariel Leading Spectral Ratio

Here we report a ratio between the spectra collected over Ariel's trailing and leading hemispheres (Figure A4).

### A.6. Results and Analyses: H<sub>2</sub>O<sub>2</sub> and Ariel's 3.6 $\mu\text{m}$ Feature

To investigate whether H<sub>2</sub>O<sub>2</sub> is present on Ariel and to measure its 3.6  $\mu\text{m}$  feature, we fitted fourth-order polynomial models to the spectra of Ariel's leading and trailing hemispheres between 3.45 and 3.7  $\mu\text{m}$  and measured the resulting continuum-subtracted features (Figure A5). We find no evidence for the 3.505  $\mu\text{m}$  H<sub>2</sub>O<sub>2</sub> feature detected on Europa (e.g., Carlson et al. 1999), Enceladus (Newman et al. 2007), and Charon (Protopapa et al. 2023, 2024; Figure A5). The continuum-subtracted data show weak features centered near 3.55 and 3.60  $\mu\text{m}$  on Ariel's trailing hemisphere. Whether these two features result from different species or are two subtle lobes of the same component is difficult to discern. We consider candidate species for the 3.55 and 3.60  $\mu\text{m}$  features in Appendix A.7.

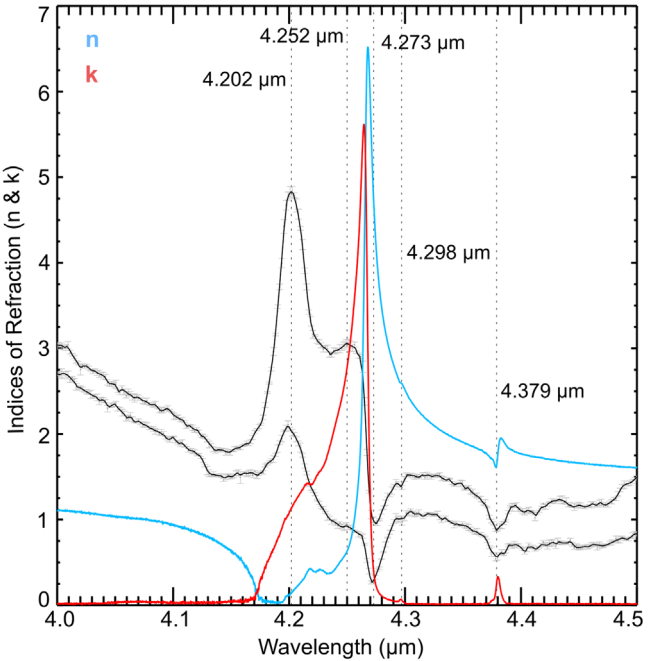


**Figure A3.** The real “ $n$ ” (blue) and imaginary “ $k$ ” (red) complex refractive indices for crystalline CO<sub>2</sub> ice measured in the laboratory at 70 K (Gerakines & Hudson 2020) compared to arbitrarily scaled spectra ( $1\sigma$  errors) of Ariel's leading and trailing (offset upward for clarity) hemispheres. Dashed lines indicate spectral features identified on Ariel that result from <sup>12</sup>CO<sub>2</sub> and <sup>13</sup>CO<sub>2</sub> ice and correspond to changes in  $n$  and  $k$  as a function of wavelength. Ariel's <sup>12</sup>CO<sub>2</sub> scattering peak starts close to 4.175  $\mu\text{m}$ , where  $k$  substantially increases above  $n$ , and ends near 4.265  $\mu\text{m}$ , where  $k$  drops off steeply and  $n$  increases above 6. The 4.30  $\mu\text{m}$  <sup>16</sup>O<sup>12</sup>C<sup>18</sup>O and 4.38  $\mu\text{m}$  <sup>13</sup>CO<sub>2</sub> features coincide with small increases in  $k$  above zero and slight dips in  $n$ .

### A.7. Discussion: Candidate Constituents

Of the 15 features we identified and measured, seven are confidently attributed to H<sub>2</sub>O, <sup>12</sup>CO<sub>2</sub>, or <sup>12</sup>CO (Table 1). The other eight are centered near 3.33, 4.02, 4.15, 4.30, 4.41, 4.47, 4.59, and 4.78  $\mu\text{m}$ . The 3.33 and 4.15  $\mu\text{m}$  features are likely dominated by CO<sub>2</sub>, but the 3.33  $\mu\text{m}$  feature may include species exhibiting C–H stretching modes (e.g., Clark et al. 2009; Grundy et al. 2002; Dartois et al. 2010), whereas the 4.15  $\mu\text{m}$  feature may also include contributions from deuterated water ice (D<sub>2</sub>O/HDO; Clark et al. 2019).

Ariel's 4.02  $\mu\text{m}$  feature might result from a broad  $\nu_1 + \nu_3$  combination mode expressed by CO<sub>3</sub>-bearing minerals (Hexter 1958; Bishop et al. 2021). Additionally, S-bearing species have been suggested to explain Callisto's broad 4.02  $\mu\text{m}$  feature, including disulfanide (HS<sub>2</sub><sup>−</sup>) and hydrogen disulfide (H<sub>2</sub>S<sub>2</sub>; Cartwright et al. 2020c), or perhaps even a wavelength-shifted sulfur dioxide (SO<sub>2</sub>) band (e.g., McCord et al. 1998). H<sub>2</sub>CO<sub>3</sub>, formed via irradiation of H<sub>2</sub>O mixed with CO<sub>2</sub>, expresses a broad band between 3.8 and 3.9  $\mu\text{m}$  due to the CO<sub>3</sub><sup>1</sup> anion (e.g., Hage et al. 1998) that might contribute to Ariel's 4.02  $\mu\text{m}$ , assuming that some process is able to shift its band center closer to 4  $\mu\text{m}$ . Conversely, Ariel's 4.02  $\mu\text{m}$  feature might be associated with the Christiansen band exhibited by <sup>12</sup>CO<sub>2</sub> ice near 4.07  $\mu\text{m}$  (seen in the CO<sub>2</sub> spectral models 1–3 shown in Figures 2 and A1). However, there is a sizable wavelength gap ( $\sim 0.05 \mu\text{m}$ ) between the Christiansen features displayed by these spectral models and Ariel's 4.02  $\mu\text{m}$  band, and it is uncertain why the Christiansen band would exhibit such a large shift, especially given that the feature is not shifted in spectra of CO<sub>2</sub>-rich TNOs (Figure A6).

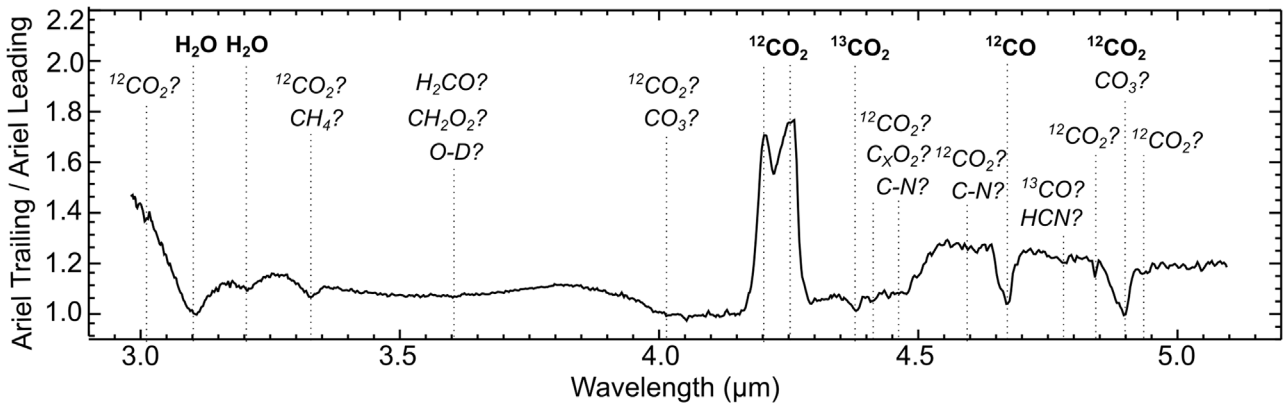


**Figure A4.** Ratio between Ariel’s trailing and leading hemispheres, normalized to 1 at 4  $\mu\text{m}$ . Dashed lines highlight the spectral features identified in the Ariel data (Figure 1) that show notable trailing/leading hemispherical asymmetries, including subtle features near 3.01, 3.33, 4.84, and 4.93  $\mu\text{m}$  that could result from deposits of  $\text{CO}_2$  ice upward of 10 mm thick (Section 4.1, Figure 4). Candidate species are described in Appendix A.7.

Because of the strength of  $\text{H}_2\text{O}$  ice absorption and the shape of the  $\text{H}_2\text{O}$  ice continuum in the 4  $\mu\text{m}$  wavelength range, exact identification of Ariel’s 4.02  $\mu\text{m}$  band center is difficult, and it may be centered at slightly shorter wavelengths, between 3.98 and 4  $\mu\text{m}$ . Similarly, Ceres exhibits a 4  $\mu\text{m}$  feature that shifts between 3.95 and 4.02  $\mu\text{m}$ , with Mg-Ca carbonates shifting its 4  $\mu\text{m}$  feature to the global average of 3.95  $\mu\text{m}$  and Na carbonates shifting the band feature to 4.02  $\mu\text{m}$  (e.g., Carrozzo et al. 2018). Therefore, if Ariel’s 4.02  $\mu\text{m}$  band is in reality centered at slightly shorter wavelengths, it would still be consistent with the broad  $\nu_1 + \nu_3$  combination mode expressed by carbonate minerals.

Ariel’s 4.30  $\mu\text{m}$  feature is embedded on the long-wavelength end of its 4.27  $\mu\text{m}$   $^{12}\text{CO}_2$  ice band and probably results from the  $\text{CO}_2$  isotopologue  $^{16}\text{O}^{12}\text{C}^{18}\text{O}$  (Bennett et al. 2010b). Although amorphous  $\text{CO}_2$  could hypothetically contribute to Ariel’s 4.30  $\mu\text{m}$  band, it is not expected to be present at Ariel’s peak surface temperatures (e.g., Escribano et al. 2013).

The 4.41 and 4.47  $\mu\text{m}$  features could result from irradiation of CO and  $\text{CO}_2$  mixtures, forming  $\text{C}_3\text{O}_2$  and other higher-order carbon chain oxides (e.g., Gerakines & Moore 2001; Strazzulla et al. 2007). Alternatively, these two features could result from irradiation of carbon oxides and ammonia ( $\text{NH}_3$ ), forming CN-bearing compounds (e.g., Strazzulla et al. 2007). The 4.41  $\mu\text{m}$  feature might also (in part) result from  $^{16}\text{O}^{13}\text{C}^{18}\text{O}$  ice (Bennett et al. 2010b).

Ariel’s 4.59  $\mu\text{m}$  feature could result from irradiation of  $\text{H}_2\text{O}$ ,  $\text{CO}_2$ , and  $\text{NH}_3$ , forming  $\text{OCN}^-$ , a key tracer of nitrogen-bearing species in the interstellar medium and protoplanetary disks (e.g., McClure et al. 2023). If  $\text{OCN}^-$  is confirmed, then a complementary  $\text{NH}_4^+$  feature should be present near 6.85  $\mu\text{m}$  (e.g., Grim et al. 1989; Palumbo et al. 2000; Bennett et al. 2010a).

Ariel’s 4.78  $\mu\text{m}$  band most likely results from  $^{13}\text{CO}$  (e.g., Bennett et al. 2010b), given that it is only detected on Ariel’s trailing side, where the  $^{12}\text{CO}$  feature is dramatically stronger (see Appendix A.8 for discussion of  $^{13}\text{CO}/^{12}\text{CO}$  isotopic ratios). Nonetheless, the  $\nu_3$  mode of hydrogen cyanide ice (HCN; e.g., Gerakines et al. 2022) might contribute to this feature as well, if nitriles are present.

Subtle features near 3.55 and 3.60  $\mu\text{m}$  on Ariel’s trailing side (Figure A5) may result from irradiation of  $\text{CO}_2$  and  $\text{H}_2\text{O}$ , possibly generating formaldehyde ( $\text{H}_2\text{CO}$ ; M. Moore et al. 2004), formic acid ( $\text{CH}_2\text{O}_2$ ; Bisschop et al. 2007), or perhaps oxalates ( $\text{C}_2\text{O}_4$ ; Applin et al. 2016). A 3.6  $\mu\text{m}$  feature on

Saturn’s moon Phoebe has also been attributed to  $\text{HDO}/\text{D}_2\text{O}$  ice (Clark et al. 2019), and perhaps deuterated water ice contributes to Ariel’s 3.6  $\mu\text{m}$  feature as well.

Finally, we identified, but did not measure, three other very subtle features centered near 3.01, 4.84, and 4.93  $\mu\text{m}$  on Ariel’s trailing hemisphere, which probably result from  $\text{CO}_2$  (Figures 4 and A4; Hansen 1997; Quirico & Schmitt 1997a).

Disentangling these various components requires follow-up laboratory experiments and associated modeling efforts. In particular, there is a need to determine whether  $\text{NH}_3$  on Ariel may have been radiolytically converted into nitriles, thereby explaining the absence of N-H stretching modes in the NIRSpec data reported here. Additionally, Ariel’s prominent double-lobed scattering peaks near 4.20 and 4.25  $\mu\text{m}$  share morphological similarities to double-lobed  $\text{CO}_2$  gas emission peaks detected at Callisto (Carlson 1999) and, more recently, the Centaur 39P/Oterma (Pinto et al. 2023). However, there is a notable wavelength shift between these  $\text{CO}_2$  gas emission peaks ( $\sim$ 4.2–4.3  $\mu\text{m}$ ) and Ariel’s scattering peaks (4.16–4.26  $\mu\text{m}$ ), which is more consistent with scattering within a thick layer of  $\text{CO}_2$  ice (Model 3 in Figure 2; Figure A3).

#### A.8. Discussion: Comparison between Ariel and $\text{CO}_2$ -bearing TNOs

Here we compare NIRSpec data of Ariel’s leading and trailing hemispheres to spectra of three TNOs observed as part of GO program 2418 (Pinilla-Alonso et al. 2021; Figure A6). These TNOs are representative of the three spectral types identified by this program (de Pra et al. 2024).

#### A.9. Discussion: $^{13}\text{CO}/^{12}\text{CO}$ Isotopic Ratios

Prior studies have used remotely sensed  $\text{H}_2\text{O}$ ,  $\text{HDO}/\text{D}_2\text{O}$  ice,  $^{12}\text{CH}_4$ ,  $^{13}\text{CH}_4$ ,  $^{12}\text{CH}_3\text{D}$ ,  $^{13}\text{CO}_2$ , and  $^{12}\text{CO}_2$  spectral features to estimate D/H and  $^{13}\text{C}/^{12}\text{C}$  isotopic ratios and gain insight into the formation conditions for different icy bodies and possible endogenic sources of material on their surfaces (Clark et al. 2019; Cartwright et al. 2024; Glein et al. 2024; Grundy et al. 2024b). Ariel’s strong  $^{12}\text{CO}_2$  scattering peaks make reliable determination of its  $^{13}\text{CO}_2/^{12}\text{CO}_2$  isotopic ratios difficult from analysis of  $\nu_3$  band parameters for  $^{12}\text{CO}_2$ , and we did not attempt to retrieve a  $^{12}\text{CO}_2$  abundance from other spectral features (e.g., at 4.90  $\mu\text{m}$ ). However, using the 4.67  $\mu\text{m}$   $^{12}\text{CO}$  and 4.78  $\mu\text{m}$  (likely)  $^{13}\text{CO}$  bands detected on

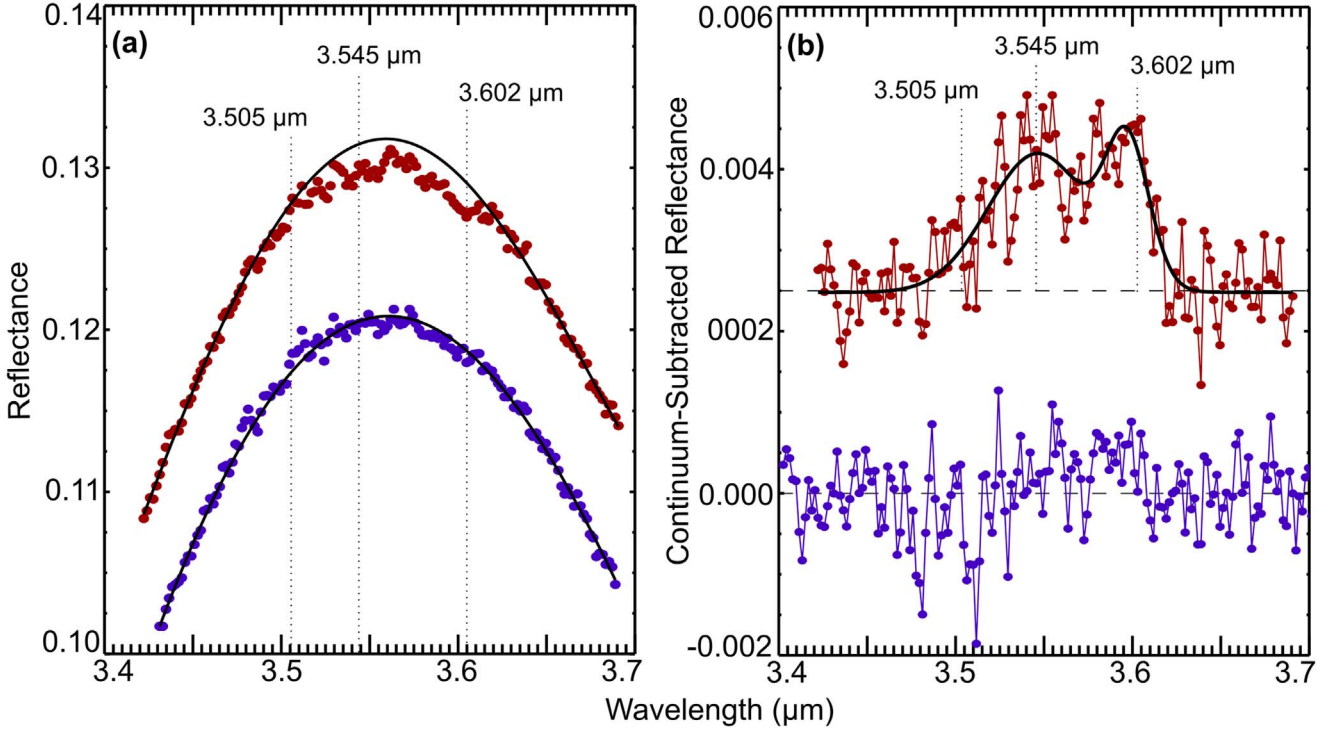


**Figure A5.** (a) Spectra of Ariel’s leading (purple) and trailing (red) hemispheres, scaled to arbitrary reflectance, fit by fourth-order polynomials simulating their continua. Dashed lines highlight the canonical central wavelength position of  $\text{H}_2\text{O}_2$  measured in the laboratory (3.505  $\mu\text{m}$ ) and two other subtle features centered near 3.545 and 3.602  $\mu\text{m}$  we have identified on Ariel’s trailing hemisphere. (b) Continuum-subtracted spectra of Ariel’s leading (purple) and trailing (red, offset upward by 0.0025) hemispheres, spanning the 3.4–3.7  $\mu\text{m}$  wavelength range. A two-Gaussian model (black) has been fit to the weak 3.55 and 3.60  $\mu\text{m}$  features observed on Ariel’s trailing hemisphere that are not seen on its leading hemisphere. Neither spectrum exhibits a 3.505  $\mu\text{m}$  band resulting from a  $\text{H}_2\text{O}_2$  combination mode (Bain & Giguère 1955).

Ariel’s trailing hemisphere, we calculated  $^{13}\text{CO}/^{12}\text{CO}$  band area and depth ratios of  $0.045 \pm 0.010$  and  $0.146 \pm 0.023$ , respectively. These results are comparable to Phoebe’s  $^{13}\text{CO}_2/\text{CO}_2$  band area ( $0.059 \pm 0.005$ ) and depth ( $0.186 \pm 0.036$ ) ratios (Cartwright et al. 2024), and the ratios on Ariel’s leading hemisphere appear qualitatively to be higher, hinting that Ariel may be significantly enhanced in  $^{13}\text{C}$  relative to “terrestrial” values ( $^{13}\text{C}/^{12}\text{C} \approx 0.010\text{--}0.012$ ) exhibited by most bodies in the inner solar system and Saturn’s rings and regular satellites (e.g., Clark et al. 2019). Whether  $^{13}\text{C}/^{12}\text{C}$  ratios derived from CO at Ariel would yield similar results to carbon isotopic ratios derived from  $\text{CO}_2$  at Phoebe is uncertain. Furthermore, CO is likely contaminated by  $\text{CO}_2$  at Ariel, and its 4.78  $\mu\text{m}$  band may be enhanced by HCN ice, assuming that nitriles are present, complicating analysis of its carbon isotopes. We report a preliminary analysis of possible  $^{13}\text{C}$  enrichment of CO and  $\text{CO}_2$  ices on Ariel in Appendix A.10. More detailed modeling of Ariel’s carbon isotopes and their spectral expression at infrared wavelengths is likely required to corroborate the CO band ratios present here, to convert band ratios to number ratios, and to fully explore their significance, e.g., in terms of formation of its carbon source material (e.g., Cartwright et al. 2024).

#### A.10. Discussion: Modeling $^{13}\text{CO}_2$ Enrichment

The pronounced 4.38  $\mu\text{m}$  absorption due to  $^{13}\text{CO}_2$  and high apparent ratios of  $^{13}\text{CO}/^{12}\text{CO}$  (assuming that CO is a radiolytic product of  $\text{CO}_2$ ) provide hints that Ariel’s surface  $\text{CO}_2$  ice is enriched in  $^{13}\text{C}$ , perhaps substantially. Here we seek to outline explanations of how  $\text{CO}_2$  could acquire a large  $^{13}\text{C}$  enrichment

via a balance between production and escape processes. We then consider a different scenario in which there is long-term isotopic fractionation of  $\text{CO}_2$  driven only by escape.

Since  $\text{CO}_2$  is concentrated on the trailing hemisphere, it may be produced by radiolytically driven oxidation reactions of, e.g., organic compounds. An alternative or complementary source of  $\text{CO}_2$  would be outgassing from the interior (e.g., a soda ocean). It may not be essential to specify the nature of the  $\text{CO}_2$  source since both options would provide  $\text{CO}_2$  with roughly similar C isotope ratios (see below). The exception would be if radiolytic processes result in isotopic fractionation, but high-energy processes are not generally associated with strong isotope effects because they usually lack selectivity. We can formulate two equations for the evolution of  $\text{CO}_2$  isotopologues in the surface environment of Ariel:

$$\frac{dN_{44}}{dt} = J_{44} - k_{44}[^{12}\text{CO}_2]_{\text{exob}}, \quad (\text{A1})$$

and

$$\frac{dN_{45}}{dt} = J_{45} - k_{45}[^{13}\text{CO}_2]_{\text{exob}}, \quad (\text{A2})$$

where  $N$  represents the number of molecules, subscripts refer to the masses of  $\text{CO}_2$  isotopologues,  $t$  stands for time,  $J$  designates production rate,  $k$  represents a rate constant for atmospheric escape, and brackets indicate the number density of the  $\text{CO}_2$  isotopologue of interest at the exobase. We adopt the classic concept of the exobase as a dividing line between nominally collisional and collisionless parts of the atmosphere. We wish to explore the simplest case in which a steady state could be

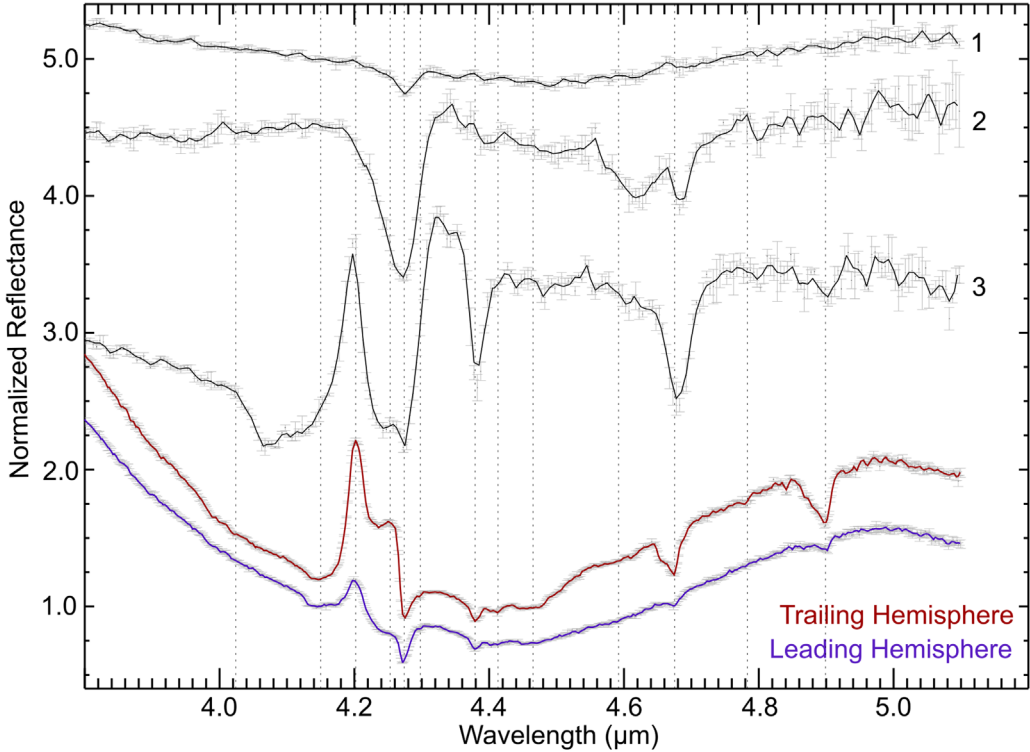


**Figure A6.** Comparison between NIRSpec IFU spectra and  $1\sigma$  uncertainties for Ariel’s leading (purple) and trailing (red) hemispheres and the TNOs 47171 Lempo (1999 TC36) (1), 2013 LU28 (2), and 2004 XA192 (3), selected to represent members of the “bowl,” “cliff,” and “double-dip” TNO types (Pinilla-Alonso et al. 2021; de Pra et al. 2024), respectively. All spectra are normalized to 1 at  $4.15 \mu\text{m}$  and offset vertically for clarity. Similar to other double-dip TNOs, 2004 XA192 exhibits strong  $^{12}\text{CO}_2$  and  $^{13}\text{CO}_2$  bands, with a  $\text{CO}_2$  scattering peak similar to Ariel’s  $4.202 \mu\text{m}$  peak. However, none of the TNOs display a strong  $4.252 \mu\text{m}$  peak, unlike Ariel. 2004 XA192 also exhibits a strong  $\sim 4.07 \mu\text{m}$  band resulting from the Christiansen effect, where  $n = 1$  and  $k = 0$  in crystalline  $\text{CO}_2$  ice (Figure A3). This Christiansen band is notably absent from the Ariel spectra and synthetic spectra composed of large grain sizes (diameters  $\sim 100 \mu\text{m}$ ; Gerakines & Hudson 2020), generated using our Hapke–Mie approach (Appendix A.2).

established. Equations (A1) and (A2) then imply that

$$\left(\frac{^{13}\text{CO}_2}{^{12}\text{CO}_2}\right)_{\text{exob}} = \frac{J_{45}/J_{44}}{k_{45}/k_{44}} = \frac{R_{\text{pro}}}{\alpha_{\text{esc}}}, \quad (\text{A3})$$

where  $R_{\text{pro}}$  stands for a ratio characteristic of a given production process and  $\alpha_{\text{esc}}$  is a fractionation factor due to  $\text{CO}_2$  loss by atmospheric escape.

We treat  $R_{\text{pro}}$  as a fixed parameter that may assume  $^{13}\text{C}/^{12}\text{C}$  ratios between those measured in primitive organic matter (1/92; Alexander et al. 2007) and carbonate minerals (1/83; Fujiya et al. 2023) in carbonaceous chondrites. The former would reflect an organic source of Ariel’s  $\text{CO}_2$  ice (e.g., carbonaceous dust), while the latter can serve as an analog for carbonate-bearing subsurface fluids that might erupt  $\text{CO}_2$ . The second value would be inherited from protosolar nebula  $\text{CO}_2$  ice that may have been accreted by Ariel at the time of its formation. The overall range of  $^{13}\text{C}/^{12}\text{C}$  ratios considered here encompasses a broad range of primordial carbon isotope ratios observed across the solar system.

We consider  $\text{CO}_2$  loss by Jeans escape. This mechanism has the potential to discriminate between species with different masses (hydrodynamic escape and sputtering are other possibilities, but they are less effective than Jeans escape at fractionating isotopes). For Jeans escape,

$$\alpha_{\text{esc}} = \sqrt{\frac{44}{45}} \left( \frac{1 + \lambda_{45}^{\text{exob}}}{1 + \lambda_{44}^{\text{exob}}} \right) \exp(\lambda_{44}^{\text{exob}} - \lambda_{45}^{\text{exob}}), \quad (\text{A4})$$

where  $\lambda_i^{\text{exob}}$  represents the escape parameter of species  $i$  at the exobase, as defined below:

$$\lambda_i^{\text{exob}} = \frac{GMm_i}{k_B T_{\text{exob}} r_{\text{exob}}}, \quad (\text{A5})$$

where  $GM = 8.23 \times 10^{10} \text{ m}^3 \text{s}^{-2}$ ;  $m_i$  corresponds to the mass of a molecule of species  $i$ ;  $k_B = 1.381 \times 10^{-23} \text{ kg m}^2 \text{s}^{-2} \text{ K}^{-1}$ ;  $T_{\text{exob}}$  denotes the exobase temperature, which is assumed to be the same as the rest of the atmosphere (as a first-order approximation); and  $r_{\text{exob}}$  indicates the distance between the exobase and the center of Ariel.

The isotope ratio at the surface can be related to that at the exobase via

$$\left(\frac{^{13}\text{CO}_2}{^{12}\text{CO}_2}\right)_{\text{surf}} = \frac{1}{\alpha_{\text{diff}}} \left(\frac{^{13}\text{CO}_2}{^{12}\text{CO}_2}\right)_{\text{exob}}, \quad (\text{A6})$$

where  $\alpha_{\text{diff}}$  denotes an isotope fractionation factor due to molecular diffusion between the surface and exobase. We assume that turbulent mixing is unimportant in Ariel’s tenuous atmosphere (i.e., the homopause is always at the surface). For an isothermal atmosphere, the diffusive fractionation factor can be computed using

$$\alpha_{\text{diff}} = \exp\left(\frac{GM(m_{45} - m_{44})(r_{\text{exob}}^{-1} - r_{\text{surf}}^{-1})}{k_B T_{\text{atm}}}\right), \quad (\text{A7})$$

where  $r_{\text{surf}} = 579 \times 10^3 \text{ m}$ . We introduce  $T_{\text{atm}}$  as a mean temperature at altitudes between the surface and exobase.

We do not know the location of Ariel's exobase. One possibility is that Ariel has a surface-bound exosphere. We can determine whether this is likely by computing the surface pressure ( $P_{\text{surf}}$ ) that would satisfy the following relation:

$$\frac{\pi d_{\text{CO}_2}^2 r_{\text{surf}}^2 P_{\text{surf}}}{GMm_{\text{CO}_2}} = 1, \quad (\text{A8})$$

where  $d_{\text{CO}_2}$  corresponds to the kinetic diameter of  $\text{CO}_2$  ( $4.53 \times 10^{-10}$  m; Haynes 2016). The pressure would need to be  $<2.8 \times 10^{-8}$  Pa for the exobase to be at the surface. If there is a sufficient  $\text{CO}_2$  supply (as suggested by the prominent  $\text{CO}_2$  features in the JWST data), then we may assume vapor pressure equilibrium to set a constraint on the maximum temperature that permits a surface-bound exosphere. We use the equation from Fray & Schmitt (2009):

$$\ln p_{\text{CO}_2,\text{sat}} \text{ (bar)} = A_0 + \sum_{j=1}^5 A_j T_{\text{surf}} \text{ (K)}^{-j}, \quad (\text{A9})$$

where  $p_{\text{CO}_2,\text{sat}}$  designates the saturation pressure of  $\text{CO}_2$  ice,  $T_{\text{surf}}$  indicates the surface temperature,  $A_0 = 14.76$ ,  $A_1 = -2571 \text{ K}$ ,  $A_2 = -7.781 \times 10^4 \text{ K}^2$ ,  $A_3 = 4.325 \times 10^6 \text{ K}^3$ ,  $A_4 = -1.207 \times 10^8 \text{ K}^4$ , and  $A_5 = 1.35 \times 10^9 \text{ K}^5$ . These parameters are applicable to temperatures between 40 and 195 K (Fray & Schmitt 2009). By calculating the saturation pressure as a function of temperature, we find that the left-hand side of Equation (A8) is  $<1$  (meaning that the mean free path is longer than the scale height) when  $T_{\text{surf}} < 71 \text{ K}$ . Hence, the exobase will be at the surface (i.e., the whole atmosphere is an exosphere) when the temperature is below 71 K; in this case,  $\alpha_{\text{diff}} = 1$ , and we can solve Equations (A3)–(A6) to determine the  $^{13}\text{CO}_2/^{12}\text{CO}_2$  ratio at the surface of Ariel.

At higher surface temperatures, the exobase will be at higher altitudes. It is not straightforward to simulate the structure of this type of atmosphere; this is an active area of research (Mogan et al. 2020). However, detailed modeling is probably not needed for our application since we lack specific values of the  $^{13}\text{CO}_2/^{12}\text{CO}_2$  ratio on Ariel to explain (see Appendix A.8). Instead, we have the more basic goal of exploring the sensitivity of the isotope ratio to unknowns that influence isotopic fractionation. The two parameters of interest here are the exobase altitude and temperature of the atmosphere. In the present treatment, we still assume that the atmosphere is isothermal, but it could have a different temperature from that of the surface. Parameters  $r_{\text{exob}}$  and  $T_{\text{atm}}$  in Equation (A7) can be varied to assess how much they could change  $\alpha_{\text{diff}}$ . Equations (A3)–(A6) can then be used to estimate the steady-state  $^{13}\text{C}/^{12}\text{C}$  ratio of Ariel's surface  $\text{CO}_2$  ice at  $T_{\text{surf}} \geq 71 \text{ K}$ . We do not account for any carbon isotopic fractionation between  $\text{CO}_2$  gas and ice at the surface, as laboratory experiments show that there is no more than  $\sim 0.4\%$  fractionation down to 130 K (Eiler et al. 2000).

As shown in Figure A7,  $\text{CO}_2$  derived from organics or carbonates can be significantly enriched in  $^{13}\text{C}$  in the surface environment of Ariel due to atmospheric escape. The predicted enrichment is about 30%, i.e., 300‰. This is very large. For comparison, biological production of  $\text{CH}_4$  from  $\text{CO}_2$  is generally considered to have a large isotope effect, with a fractionation that can reach  $\sim 80\%$  (Miljković & Etiope 2018). Our predictions appear to be qualitatively consistent with the ease of finding features from  $^{13}\text{CO}_2$  and  $^{13}\text{CO}$  in the JWST

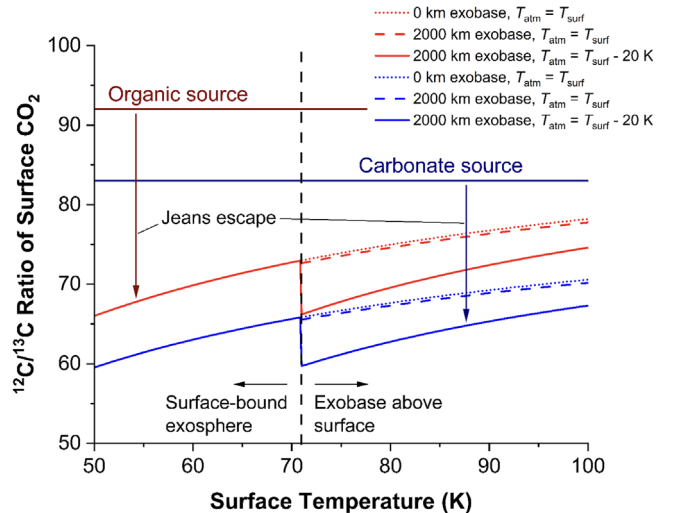


**Figure A7.** Carbon isotopic composition (light/heavy) of steady-state  $\text{CO}_2$  at the surface of Ariel. These results show how input values of the  $^{12}\text{C}/^{13}\text{C}$  ratio from organics or carbonates (dark horizontal lines) are shifted downward by Jeans escape. For each set of lighter-colored curves, we consider a case with a surface-bound exosphere at all temperatures and  $T_{\text{atm}} = T_{\text{surf}}$  (dotted), a case where the exobase altitude has been increased to 2000 km while keeping  $T_{\text{atm}} = T_{\text{surf}}$  (dashed), and a case where the exobase altitude remains at 2000 km but the atmospheric temperature is 20 K lower than the surface temperature. The offsets for these cases are intended to be illustrative, and other values are possible.

data. It can be seen in Figure A7 that increasing the exobase altitude may not have a significant effect on the isotope ratio, at least up to 2000 km. The atmospheric temperature can have a larger effect in enriching  $^{13}\text{CO}_2$  at the surface. Yet its effect on diffusive fractionation seems less important than Jeans fractionation, which is responsible for most of the total fractionation in our test cases. Isotopic fractionation by diffusion is limited by large scale heights of Ariel's atmosphere.

The spurious drops at 71 K in Figure A7 arise from the arbitrary assumption that the exobase is at the surface at temperatures below 71 K and at an altitude of 2000 km at higher temperatures. Although assuming a constant exobase level isolates its effects on the  $^{13}\text{C}/^{12}\text{C}$  ratio, in a more realistic model the exobase would progressively increase in altitude from the surface level with increasing surface temperature and pressure.

Whether a steady state is reached is an open question. In another end-member scenario, one can assume progressive depletion of a primordial surface  $\text{CO}_2$  inventory, as a fraction sublimates each summer to form gaseous  $\text{CO}_2$  that undergoes isotopic fractionation due to Jeans escape. From Equation (A4),  $\alpha_{\text{esc}} \approx 0.72$  assuming  $T_{\text{surf}} = 55 \text{ K}$  and a surface-bound exobase, or 0.78 at  $T_{\text{surf}} = 71 \text{ K}$ . Assuming escape of a modest fraction  $f_{\text{esc}} = 0.1 \text{ ppm}$  of all the surface  $\text{CO}_2$  each Uranian year, the  $^{13}\text{C}/^{12}\text{C}$  ratio of primordial  $\text{CO}_2$  would increase by a factor of  $(f_{\text{esc}}/\alpha_{\text{esc}})(4.57 \times 10^9/86) \approx 7$  (i.e., 7000‰) over the 4.57 Gyr of solar system history, assuming a constant orbital period for Uranus of 86 Earth years. This requires  $\text{CO}_2$  to be gaseous for part, and only part, of the Uranian year.

This calculated enrichment in  $^{13}\text{C}$  is even more considerable than in the steady-state scenario, as the ever-increasing  $^{13}\text{C}/^{12}\text{C}$  ratio of the surface  $\text{CO}_2$  is not diluted by constantly replenishing  $\text{CO}_2$  with a canonical  $^{13}\text{C}/^{12}\text{C} \approx 1/90$ . This enrichment is of the same order of magnitude as the factors

of  $\approx 4.5$  and 15 inferred, respectively, from the band area and depth ratios of  $^{13}\text{CO}$  and  $^{12}\text{CO}$  on Ariel (see Appendix A.9). The corresponding  $f_{\text{esc}} = 0.1$  ppm is consistent with a  $\text{CO}_2$  initial inventory  $(1 + f_{\text{esc}})^{4.5e9/86} \approx 200$  times greater than the present-day surface abundance; i.e., equivalent layer thicknesses on the order of 10 m or larger based on the  $>10$  mm present-day deposit thicknesses discussed in Section 4.1. Compared to water inventories equivalent to global ice shell thicknesses of 100 km or more (e.g., Castillo-Rogez et al. 2023), this appears compatible with bulk  $\text{CO}_2/\text{H}_2\text{O}$  abundance ratios of less than a few mol% based on observations of comets (Mumma & Charnley 2011), which may be indicative of the composition of icy material accreted by Ariel. Such bulk compositions allow for greater values of  $f_{\text{esc}}$ , which would be required to obtain the same  $^{13}\text{C}$  enrichment in intermediate scenarios involving both primordial inventory depletion and some degree of endogenic (and, for CO, radiolytic) replenishment. We leave to future work the questions of what the absolute rate of  $\text{CO}_2$  escape might have been through time, whether it is consistent with the removal of almost all of Ariel's surface  $\text{CO}_2$  inventory, and how much radiolytic production may be implied to account for trailing versus leading hemisphere differences in the apparent abundance of  $\text{CO}_2$ . Future constraints on the  $^{18}\text{O}/^{16}\text{O}$  ratio may enable further discrimination between steady-state and limited replenishment scenarios, as the larger mass difference between  $^{16}\text{OC}^{18}\text{O}$  and  $^{16}\text{OC}^{16}\text{O}$  can be expected to magnify the degree of fractionation.

The models outlined above may have more general applicability to other outer solar system bodies with abundant  $^{13}\text{CO}_2$ . In addition to the phenomena considered in this appendix, it may be useful to consider how lateral heterogeneities in the availability of  $\text{CO}_2$  ice, seasonal effects on surface temperatures, kinetic inhibition of  $\text{CO}_2$  sublimation, and possible vapor pressure isotope effects at low temperatures might come together to create a rich isotope geochemistry that we are just beginning to glimpse.

## ORCID iDs

- Richard J. Cartwright <https://orcid.org/0000-0002-6886-6009>  
 Bryan J. Holler <https://orcid.org/0000-0002-6117-0164>  
 William M. Grundy <https://orcid.org/0000-0002-8296-6540>  
 Stephen C. Tegler <https://orcid.org/0000-0002-6794-495X>  
 Marc Neveu <https://orcid.org/0000-0002-6220-2869>  
 Ujjwal Raut <https://orcid.org/0000-0002-6036-1575>  
 Christopher R. Glein <https://orcid.org/0000-0002-2161-4672>  
 Tom A. Nordheim <https://orcid.org/0000-0001-5888-4636>  
 Joshua P. Emery <https://orcid.org/0000-0001-9265-9475>  
 Julie C. Castillo-Rogez <https://orcid.org/0000-0003-0400-1038>  
 Eric Quirico <https://orcid.org/0000-0003-2768-0694>  
 Silvia Protopapa <https://orcid.org/0000-0001-8541-8550>  
 Chloe B. Beddingfield <https://orcid.org/0000-0001-5048-6254>  
 Matthew M. Hedman <https://orcid.org/0000-0002-8592-0812>  
 Katherine de Kleer <https://orcid.org/0000-0002-9068-3428>  
 Riley A. DeColibus <https://orcid.org/0000-0002-1647-2358>  
 Anastasia N. Morgan <https://orcid.org/0000-0001-5932-9570>

- Ryan Wochner <https://orcid.org/0009-0007-4457-0557>  
 Kevin P. Hand <https://orcid.org/0000-0002-3225-9426>  
 Geronimo L. Villanueva <https://orcid.org/0000-0002-2662-5776>  
 Sara Faggi <https://orcid.org/0000-0003-0194-5615>  
 Noemi Pinilla-Alonso <https://orcid.org/0000-0002-2770-7896>  
 David E. Trilling <https://orcid.org/0000-0003-4580-3790>  
 Michael M. Mueller <https://orcid.org/0000-0003-3217-5385>

## References

- Alexander, C. O., Fogel, M., Yabuta, H., & Cody, G. 2007, *GeCoA*, **71**, 4380  
 Applin, D. M., Izawa, M. R., & Cloutis, E. A. 2016, *Icar*, **278**, 7  
 Bain, O., & Giguère, P. A. 1955, *CaJCh*, **33**, 527  
 Bauer, J. M., Roush, T. L., Geballe, T. R., et al. 2002, *Icar*, **158**, 178  
 Beddingfield, C., Li, C., Atreya, S., et al. 2020, arXiv:2007.11063  
 Beddingfield, C. B., & Cartwright, R. J. 2021, *Icar*, **367**, 114583  
 Beddingfield, C. B., Cartwright, R. J., Leonard, E., Nordheim, T., & Scipioni, F. 2022, *PSJ*, **3**, 106  
 Bennett, C., Jones, B., Knox, E., et al. 2010a, *ApJ*, **723**, 641  
 Bennett, C. J., Jamieson, C. S., & Kaiser, R. I. 2010b, *PCCP*, **12**, 4032  
 Bini, R., Salvi, P., Schettino, V., & Jodl, H.-J. 1991, *PhLA*, **157**, 273  
 Bishop, J., King, S., Lane, M., et al. 2021, *E&SS*, **8**, e2021EA001844  
 Bisschop, S., Fuchs, G., Boogert, A., van Dishoeck, E., & Linnartz, H. 2007, *A&A*, **470**, 749  
 Bockelee-Morvan, D., Lellouch, E., Poch, O., et al. 2024, *A&A*, **681**, A27  
 Bohlin, R. C., & Landolt, A. U. 2015, *AJ*, **149**, 122  
 Bohren, C., & Huffman, D. 1983, Absorption and scattering of light by small particles (New York: Wiley)  
 Böker, T., Beck, T., Birkmann, S., et al. 2023, *PASP*, **135**, 038001  
 Brown, M. E., & Calvin, W. M. 2000, *Sci*, **287**, 107  
 Brown, M. E., & Fraser, W. C. 2023, *PSJ*, **4**, 130  
 Brown, R. H., & Cruikshank, D. P. 1983, *Icar*, **55**, 83  
 Buie, M., & Grundy, W. 2000, *Icar*, **148**, 324  
 Bushouse, H., Eisenhamer, J., Dencheva, N., Davies, J., & Greenfield, P. e. a. 2023, JWST Calibration Pipeline, v1.11.0, Zenodo, doi:10.5281/zenodo.8067394  
 Carlson, R., Anderson, M., Johnson, R., et al. 1999, *Sci*, **283**, 2062  
 Carlson, R. W. 1999, *Sci*, **283**, 820  
 Carrozzo, F. G., De Sanctis, M. C., Raponi, A., et al. 2018, *SciA*, **4**, e1701645  
 Cartwright, R., Beddingfield, C., Nordheim, T., et al. 2021, *PSJ*, **2**, 120  
 Cartwright, R. J., Beddingfield, C. B., Nordheim, T. A., et al. 2020a, *ApJL*, **898**, L22  
 Cartwright, R. J., DeColibus, R. A., Castillo-Rogez, J. C., et al. 2023, *PSJ*, **4**, 42  
 Cartwright, R. J., Emery, J. P., Grundy, W. M., et al. 2020b, *Icar*, **338**, 113513  
 Cartwright, R. J., Emery, J. P., Pinilla-Alonso, N., et al. 2018, *Icar*, **314**, 210  
 Cartwright, R. J., Emery, J. P., Rivkin, A. S., Trilling, D. E., & Pinilla-Alonso, N. 2015, *Icar*, **257**, 428  
 Cartwright, R. J., Nordheim, T. A., Cruikshank, D. P., et al. 2020c, *ApJL*, **902**, L38  
 Cartwright, R. J., Nordheim, T. A., DeColibus, R. A., et al. 2022, *PSJ*, **3**, 8  
 Cartwright, R. J., Villanueva, G. L., Holler, B. J., et al. 2024, *PSJ*, **5**, 27  
 Castillo-Rogez, J., Daswani, M., Glein, C., Vance, S., & Cochrane, C. 2022, *GeoRL*, **49**, e2021GL097256  
 Castillo-Rogez, J., Neveu, M., McSween, H. Y., et al. 2018, *M&PS*, **53**, 1820  
 Castillo-Rogez, J., Weiss, B., Beddingfield, C., et al. 2023, *JGRE*, **128**, e2022JE007432  
 Clark, R. N., Brown, R. H., Cruikshank, D. P., & Swayze, G. A. 2019, *Icar*, **321**, 791  
 Clark, R. N., Curchin, J. M., Hoefen, T. M., & Swayze, G. A. 2009, *JGRE*, **114**, 19  
 Clark, R. N., & Lucey, P. G. 1984, *JGRB*, **89**, 6341  
 Clark, R. N., & Roush, T. L. 1984, *JGRB*, **89**, 6329  
 Cohen, I. J., Beddingfield, C., Chancia, R., et al. 2022, *PSJ*, **3**, 58  
 Cook, J. C., Dalle Ore, C. M., Protopapa, S., et al. 2018, *Icar*, **315**, 30  
 Cook, J. C., Protopapa, S., Dalle Ore, C. M., et al. 2023, *Icar*, **389**, 115242  
 Cooke, I. R., Fayolle, E. C., & Öberg, K. I. 2016, *ApJ*, **832**, 5  
 Cruikshank, D., Pilcher, C. B., & Morrison, D. 1977, *ApJ*, **217**, 1006  
 Dartois, E. 2011, *Icar*, **212**, 950  
 Dartois, E., Deboffle, D., & Bouzit, M. 2010, *A&A*, **514**, A49

- de Pra, M., Hénault, E., Pinilla-Alonso, N., et al. 2024, *NatAs*, Advanced Online Publication
- De Sanctis, M. C., Raponi, A., Ammannito, E., et al. 2016, *Natur*, **536**, 54
- DeColibus, R. A., Chanover, N. J., & Cartwright, R. J. 2022, *PSJ*, **3**, 119
- DeColibus, R. A., Chanover, N. J., & Cartwright, R. J. 2023, *PSJ*, **4**, 191
- Delitsky, M. L., & Lane, A. L. 1998, *JGRE*, **103**, 31391
- Eiler, J. M., Kitchen, N., & Rahn, T. A. 2000, *GeCoA*, **64**, 733
- Emery, J., Wong, I., Brunetto, R., et al. 2024, *Icar*, **414**, 116017
- Escribano, R. M., Muñoz Caro, G. M., Cruz-Díaz, G. A., Rodríguez-Lazcano, Y., & Maté, B. 2013, *PNAS*, **110**, 12899
- Fray, N., & Schmitt, B. 2009, *P&SS*, **57**, 2053
- Fujiya, W., Kawasaki, N., Nagashima, K., et al. 2023, *NatGe*, **16**, 675
- Gerakines, P., & Moore, M. 2001, *Icar*, **154**, 372
- Gerakines, P., Moore, M. H., & Hudson, R. L. 2000, *A&A*, **357**, 793
- Gerakines, P. A., & Hudson, R. L. 2020, *ApJ*, **901**, 52
- Gerakines, P. A., Materese, C. K., & Hudson, R. L. 2023, *MNRAS*, **522**, 3145
- Gerakines, P. A., Yarnall, Y. Y., & Hudson, R. L. 2022, *MNRAS*, **509**, 3515
- Glein, C. R., Baross, J. A., & Waite, J. H., Jr. 2015, *GeCoA*, **162**, 202
- Glein, C. R., Grundy, W. M., Lunine, J. I., et al. 2024, *Icar*, **412**, 115999
- Glein, C. R., & Waite, J. H., Jr. 2018, *Icar*, **313**, 79
- Grim, R., Greenberg, J., De Groot, M., et al. 1989, *A&AS*, **78**, 161
- Grundy, W., Binzel, R., Buratti, B., et al. 2016, *Sci*, **351**, aad9189
- Grundy, W., Schmitt, B., & Quirico, E. 2002, *Icar*, **155**, 486
- Grundy, W., Tegler, S., Steckloff, J., et al. 2024a, *Icar*, **410**, 115767
- Grundy, W., Wong, I., Glein, C., et al. 2024b, *Icar*, **411**, 115923
- Grundy, W., Young, L., Spencer, J., et al. 2006, *Icar*, **184**, 543
- Grundy, W., Young, L., & Young, E. 2003, *Icar*, **162**, 222
- Hage, W., Liedl, K. R., Hallbrucker, A., & Mayer, E. 1998, *Sci*, **279**, 1332
- Hanel, R., Conrath, B., Flasar, F., et al. 1986, *Sci*, **233**, 70
- Hansen, G. B. 1997, *AdSpR*, **20**, 1613
- Hansen, G. B. 2005, *JGRE*, **110**, 18
- Hapke, B. 2012, Theory of Reflectance and Emittance Spectroscopy (Cambridge: Cambridge Univ. Press)
- Haynes, W. M. 2016, CRC Handbook of Chemistry and Physics (Boca Raton, FL: CRC Press)
- Hendrix, A. R., Hurford, T. A., Barge, L. M., et al. 2019, *AsBio*, **19**, 1
- Hexter, R. 1958, *AcSpE*, **10**, 281
- Hibbitts, C., Klemaszewski, J., McCord, T., Hansen, G., & Greeley, R. 2002, *JGRE*, **107**, 14
- Hibbitts, C., McCord, T., & Hansen, G. 2000, *JGRE*, **105**, 22541
- Holler, B., Young, L., Grundy, W., & Olkin, C. 2016, *Icar*, **267**, 255
- Hudson, R., Moore, M., & Gerakines, P. 2001, *ApJ*, **550**, 1140
- Jakobsen, P., Ferruit, P., de Oliveira, C. A., et al. 2022, *A&A*, **661**, A80
- Johnson, R., Carlson, R., Cooper, J., et al. 2004, in Jupiter: The Planet, Satellites and Magnetosphere, ed. F. Bagenal, T. E. Dowling, & W. B. McKinnon (Cambridge: Cambridge Univ. Press), 485
- Kirchoff, M. R., Dones, L., Singer, K., & Schenk, P. 2022, *PSJ*, **3**, 42
- Leonard, E. J., Elder, C., Nordheim, T. A., et al. 2021, *PSJ*, **2**, 174
- Licandro, J., Pinilla-Alonso, N., Holler, B., et al. 2023, Surface Composition of Centaurs: insights into the thermal evolution of TNOs, doi: [10.21203/rs.3.rs-3606680/v1](https://doi.org/10.21203/rs.3.rs-3606680/v1)
- Mamo, B., Brody, J., Teolis, B., et al. 2023, Annual Meeting of the Division for Planetary Sciences, **55**, 220.08
- Mastrapa, R., Sandford, S., Roush, T., Cruikshank, D., & Dalle Ore, C. 2009, *ApJ*, **701**, 1347
- McClure, M. K., Rocha, W., Pontoppidan, K., et al. 2023, *NatAs*, **7**, 12
- McCord, T. A., Hansen, G., Clark, R., et al. 1998, *JGRE*, **103**, 8603
- Menten, S. M., Sori, M. M., Bramson, A. M., et al. 2023, Uranus Flagship: Investigations and Instruments for Cross-Discipline Science Workshop, LPI Contribution, **2808**, 8144
- Mifsud, D. V., Kaňuchová, Z., Ioppolo, S., et al. 2022, *JMoSp*, **385**, 111599
- Milkov, A. V., & Etiope, G. 2018, *OrGeo*, **125**, 109
- Morgan, S. R. C., Tucker, O. J., Johnson, R. E., & Sreenivasan, K. R. 2020, *Icar*, **352**, 113932
- Moore, J. M., Chapman, C. R., Bierhaus, E. B., et al. 2004, in Jupiter: The Planet, Satellites, Magnetosphere, ed. F. Bagenal, T. E. Dowling, & W. B. McKinnon, Vol. 1 (Cambridge: Cambridge Univ. Press), 397
- Moore, M., Hudson, R., & Ferrante, R. 2004, The First Decadal Review of the Edgeworth-Kuiper Belt (Berlin: Springer), 291
- Moore, M., & Khanna, R. 1991, *AcSpA*, **47**, 255
- Moore, M. H., Ferrante, R., Hudson, R., & Stone, J. 2007, *Icar*, **190**, 260
- Mumma, M. J., & Charnley, S. B. 2011, *ARA&A*, **49**, 471
- National Academies of Sciences, Engineering, and Medicine 2023, Origins, Worlds, and Life: Planetary Science and Astrobiology in the Next Decade. 1 (Washington, DC: The National Academies Press).
- Ness, N. F., Acuna, M. H., Behannon, K. W., et al. 1986, *Sci*, **233**, 85
- Neveu, M., Desch, S. J., Shock, E. L., & Glein, C. R. 2015, *Icar*, **246**, 48
- Newman, S., Buratti, B., Jaumann, R., Bauer, J., & Momary, T. 2007, *ApJL*, **670**, L143
- Nordheim, T., Hand, K. P., Paranicas, C., et al. 2017, *Icar*, **286**, 56
- Palumbo, M., Strazzulla, G., Pendleton, Y., & Tielens, A. 2000, *ApJ*, **534**, 801
- Peter, J. S., Nordheim, T. A., & Hand, K. P. 2024, *NatAs*, **8**, 164
- Pinilla-Alonso, N., Bannister, M., Brunetto, R., et al. 2021, DiSCo-TNOs: Discovering the composition of the trans-Neptunian objects, icy embryos for planet formation, JWST Proposal, Cycle 1, ID. 2418
- Pinto, O. H., Kelley, M., Villanueva, G., et al. 2023, *PSJ*, **4**, 208
- Postberg, F., Kempf, S., Schmidt, J., et al. 2009, *Natur*, **459**, 1098
- Postberg, F., Sekine, Y., Klenner, F., et al. 2023, *Natur*, **618**, 489
- Protopapa, S., Cook, J., Grundy, W., et al. 2021, Pluto System after New Horizons (Tucson, AZ: Univ. of Arizona Press)
- Protopapa, Silvia, Stansberry, John, Wong, Ian, et al. 2023, Annual Meeting of the Division for Planetary Sciences, **55**, 301.02
- Protopapa, S., Raut, U., Wong, I., et al. 2024, NatCo, in press
- Quirico, E., & Schmitt, B. 1997a, *Icar*, **127**, 354
- Quirico, E., & Schmitt, B. 1997b, Near-IR optical constants of crystalline CO<sub>2</sub> ice at 179 K completed with 28K data. SSHADE/GhoSST (OSUG Data Center, Dataset/Spectral Data), doi: [10.26302/SSHADE/EXPERIMENT\\_BS\\_20130215\\_001](https://doi.org/10.26302/SSHADE/EXPERIMENT_BS_20130215_001)
- Raponi, A., De Sanctis, M. C., Carrozzo, F. G., et al. 2019, *Icar*, **320**, 83
- Rauscher, B. J. 2024, *PASP*, **136**, 015001
- Raut, U., & Baragiola, R. 2013, *ApJ*, **772**, 53
- Raut, U., Fulvio, D., Loeffler, M., & Baragiola, R. 2012, *ApJ*, **752**, 159
- Rivkin, A., Volquardsen, E., & Clark, B. 2006, *Icar*, **185**, 563
- Rouleau, F., & Martin, P. 1991, *ApJ*, **377**, 526
- Sandford, S., Allamandola, L., Tielens, A., & Valero, G. 1988, *ApJ*, **329**, 498
- Smith, B. A., Soderblom, L., Beebe, R., et al. 1986, *Sci*, **233**, 43
- Sori, M. M., Bapst, J., Bramson, A. M., Byrne, S., & Landis, M. E. 2017, *Icar*, **290**, 1
- Souza-Feliciano, A., Holler, B., Pinilla-Alonso, N., et al. 2024, *A&A*, **681**, L17
- Steckloff, J. K., Goldstein, D., Trafton, L., Varghese, P., & Prem, P. 2022, *Icar*, **384**, 115092
- Strazzulla, G., Brucato, J., Palumbo, M., & Spinella, F. 2007, *MmSAI*, **78**, 681
- Taylor, J. 1997, Introduction to Error Analysis, the Study of Uncertainties in Physical Measurements (New York: Univ. Science Books)
- Tegler, S., Grundy, W., Loeffler, M., et al. 2024, *PSJ*, **5**, 31
- Tosi, F., Mura, A., Cofano, A., et al. 2024, *NatAs*, **8**, 82
- Villanueva, G., Hammel, H., Milam, S., et al. 2023, *Sci*, **381**, 1305
- Wong, I., Brown, M. E., Emery, J. P., et al. 2024, *PSJ*, **5**, 87
- Wong, I., Hines, D., Brunetto, R., et al. 2023, AAS/Division for Planetary Sciences Meeting Abstracts, **55**, 401.08